Local optogenetic NMYII activation within the zebrafish neural rod results in long-range, asymmetric force propagation

Helena A Crellin[1], Chengxi Zhu[2]*, Guillermo Serrano-Nájera[3]*, Amelia Race[1], Kevin O'Holleran[2], Martin O Lenz[2,4], Clare E Buckley[1,5]‡

*** These authors contributed equally**
‡ Author for correspondence
[1]Department of Physiology, Development and Neuroscience, University of Cambridge, Cambridge, UK.
[2]Cambridge Advanced Imaging Centre, University of Cambridge, Anatomy Building, Cambridge, UK.
[3]Department of Genetics, University of Cambridge, Cambridge, UK.
[4]Sainsbury Laboratory, University of Cambridge, Cambridge, UK.
[5]Faculty of Biology, Medicine & Health, University of Manchester, Manchester, UK

Abstract
How do cellular forces propagate through tissue to allow large-scale morphogenetic events? To investigate this question, we use an *in vivo* optogenetic approach to reversibly manipulate actomyosin contractility at depth within the developing zebrafish neural rod. Contractility was induced along the lateral cortices of a small patch of developing neural epithelial progenitor cells, resulting in a shortening of these cells along their mediolateral axis. Imaging the immediate response of surrounding tissue uncovered a long-range, tangential, and elastic tissue deformation along the anterior-posterior axis. Unexpectedly, this was highly asymmetric, propagating in either the anterior or the posterior direction in response to local gradients in optogenetic activation. The degree of epithelialisation did not have a significant impact on the extent of force propagation via lateral cortices. We also uncovered a dynamic oscillatory expansion and contraction of the tissue along the anterior-posterior axis, with wavelength matching rhombomere length. Together, this study suggests dynamic and wave-like propagation of force between rhombomeres along the anterior-posterior axis. It also suggests that cell generated forces are actively propagated over long distances within the tissue, and that local anisotropies in tissue organisation and contractility may be sufficient to drive directional force propagation.

Introduction
Long-range force propagation is necessary for morphogenetic processes such as convergence extension, tissue folding and tissue elongation. One important source of subcellular force generation within developing epithelial tissue is the actomyosin complex. The coordinated balance between force generation by this complex and the transmission of this force via cadherin-based cell-cell adhesions is integral to initiating morphogenesis at the tissue scale (Clarke & Martin, 2021; Heisenberg & Bellaiche, 2013). Specific patterns of subcellular force at the apical surfaces and apical-lateral junctions have been shown to facilitate morphogenesis at the whole embryo scale. For example, the anisotropic contractility of planar-polarised actomyosin enables *Drosophila* germband extension (Bertet *et al*, 2004; Dicko *et al*, 2017; Rauzi *et al*, 2010; Simoes Sde *et al*, 2010; Zallen & Wieschaus, 2004). However, transmission of forces between the lateral sides of cells is also potentially instrumental in facilitating complex morphogenesis. For example, light sheet imaging of the columnar *Drosophila* germband epithelium revealed that NMYII-dependent contractile oscillations occur at points throughout the apical-basal axis of cells, where they can initiate topology change along the cell length (Vanderleest *et al*, 2024). In pseudostratified epithelia such as the neuroepithelium, each cell is in contact with multiple and differing neighbours along its apical-basal length (Gomez *et al*, 2021). This means that forces transmitted laterally have the potential to transmit to more neighbours than those at the apical surfaces.

Until recently, a major limitation in studying *in vivo* force transmission has been the inability to manipulate mechanics or signalling with sufficient spatiotemporal control. The advent of *in vivo*

optogenetic approaches has huge potential to unlock previously unreachable mechanisms in biology. It allows the role of subcellular and cellular events to be investigated at the tissue scale within complex organisms, via non-invasive light patterning (Crellin & Buckley, 2024; Krueger *et al*, 2019). This has started to allow researchers to specifically probe the role of actomyosin during morphogenesis with high spatiotemporal precision. These studies have mainly focused on actomyosin networks within polarised epithelia. For example, optogenetic manipulation of Rho1 activity in the *Drosophila* embryo demonstrated that both apical constriction and basal relaxation are required to enable tissue folding during gastrulation (Izquierdo *et al*, 2018; Krueger *et al*, 2018). It also demonstrated that NMYII is dynamically recruited to junctions under strain (Gustafson *et al*, 2022). A recent study has used similar optogenetic constructs to demonstrate that a balance between contractility and anisotropic subcellular localisation is required for productive cell-cell rearrangement and tissue fluidity during *Drosophila* germ band epithelial elongation (Herrera-Perez *et al*, 2023). Very recently, optogenetic activation of RhoA at lateral membranes has uncovered that apical-basal cell shortening can contribute to tissue furrowing during *Drosophila* gastrulation (Countryman *et al*, 2024).

An exciting advance in our understanding of lateral force propagation between epithelial cells was achieved via optogenetic activation of actomyosin contractility in one cell of a micropatterned doublet, and measurement of the mechanical response of the second (receiver) cell (Ruppel *et al*, 2023). This demonstrated that the receiver cell shows an active contractile response to force from the first cell, which enables signal strength to be maintained over distance. Interestingly, the study also found that the response of the receiver cell was stronger when the force propagation was perpendicular to the axis of mechano-structural polarisation. This active propagation of force was also seen in small cell clusters. However, until recently it has been difficult to directly measure how lateral cell-scale forces propagate at the tissue scale, particularly in deep, physiologically relevant 3D environments. It is also not clear how force propagation might be affected by the cellular state of the tissue – for example, does tangential force propagate differently between cells that are fully epithelial compared with those that are still more mesenchymal in state?

A tractable tissue in which to investigate these questions is the developing zebrafish hindbrain. During zebrafish hindbrain development, neural epithelial progenitor cells elongate and interdigitate along their mediolateral axis. During this process, they undergo a mesenchymal to epithelial transition, forming a polarised midline along the centre of the initially solid organ primordium (Buckley *et al*, 2013), from which two opposing apical-lateral junctional belts emerge (Symonds *et al*, 2020). This precedes the opening of a fluid-filled neural tube via hollowing. Preceding and overlapping with medial-lateral polarisation, the embryo also undergoes convergence and extension, becoming thinner along the mediolateral axis and longer along the tangential anterior-posterior (AP) axis (Williams & Solnica-Krezel, 2020). During this process, the tissue undergoes divergent anterior-posterior expansive strain and medial-lateral compressive strain, coordinated over very large areas (Bhattacharya *et al*, 2021). We aimed to understand how rapid changes in cellular-level forces might underly such larger scale and slower movements at the tissue level. We therefore sought to uncover how forces propagate during neural rod polarisation, at depth within the zebrafish hindbrain. We investigated 1) the extent and direction that cellular force propagates in the tissue, and 2) whether the strain experienced by the tissue in response to cellular force differs over space (anterior-posterior axis) and time (mesenchymal-epithelial state of the cells). To do this, we further developed an *in vivo* optogenetic approach within zebrafish using the Phytochrome system (Buckley, 2019; Buckley *et al*, 2016) to enable reversible control of actomyosin contractility deep within the developing hindbrain. Using a digital mirror device light pattering system coupled with a spinning disc microscope, we induced contractility along the mediolateral aspect of neuroepithelial cells to investigate force propagation via lateral adhesions, independently to the developing apical-lateral junctional belt at the tissue midline.

Results

Optogenetic membrane localisation of DH domain of Arhgef12a specifically activates RhoA and induces NMYII phosphorylation within a zebrafish transgenic line.

We first aimed to devise an optogenetic approach to activate actomyosin contractility within zebrafish embryos with minimal background activation. We chose to use a similar approach to that used in cell culture by the Glotzer lab (Wagner & Glotzer, 2016). Here, they used the TuLIP optogenetic system to recruit the catalytic Dbl homology (DH) domain of the RhoA guanine nucleotide exchange factor (GEF) ARHGEF12a (also known as Leukaemia-associated Rho GEF, 'LARG') to particular membrane regions of cells. This was sufficient to induce ectopic cleavage furrows within non-adherent interphase HeLa cells (Wagner & Glotzer, 2016). The Dbl homology-pleckstrin homology (DH-PH) domain for LARG is highly specific for RhoA, B and C, being inactive towards other Rho family members, and also has very high catalytic activity (Jaiswal *et al*, 2011). This makes ARHGEF12a a good candidate for specific RhoA activation. Similar optogenetic LARG-induced cleavage furrows were later shown to occur via plasma membrane flow in response to increased actomyosin contractility (Castillo-Badillo *et al*, 2020), demonstrating that activation of RhoA by this method is a good approach to initiate actomyosin contractility.

We previously demonstrated that the Phytochrome optogenetic system can be successfully used, *in vivo,* within zebrafish embryos, to reversibly control protein localisation with high spatiotemporal resolution (Buckley *et al.*, 2016). Here, we generated a stable transgenic zebrafish line, *Tg(ubb:Ath.Pif6-EGFP-arhgef12a),* (*Tg(Pif6-EGFP-Larg)* for short (see methods)). This line expresses a fusion protein consisting of the Arabidopsis phytochrome interacting factor Pif6, linked to the zebrafish-specific DH domain of Larg, driven by a ubiquitous promoter. Unlike many optogenetic approaches (Hallett *et al*, 2016), this minimal construct did not appear to cause background activation. One exception to this was in enveloping layer (EVL) cells, in which Pif6-Larg-EGFP sometimes had constitutive membrane or punctate localisation paired with EVL cell morphological defects (Figure S1). This is likely due to the very high surface area to volume ratio of EVL cells, causing stochastic contact between cytoplasmic Larg and the cell membrane.

To achieve optogenetic heterodimerisation, we introduced a membrane-associated version of Phytochrome B (PHYB), the binding partner of Pif6, via mRNA injections of *PhyB-MCh-Caax or PhyB-Caax.* This was co-injected with the chromophore phycocyanobilin (PCB) into one cell of 4-32 cell stage embryos, as previously published (Buckley, 2019; Buckley *et al.*, 2016). Expressing PHYB in this way enabled the titration of PHYB anchor copy number, since higher relative expression of optogenetic 'anchors' is important for efficient recruitment of the 'bait' (Buckley, 2019; Crellin & Buckley, 2024; Natwick & Collins, 2021). Varying the developmental stage at which mRNA was injected allowed us to control the extent of optogenetic manipulation by altering the mosaicism of PHYB expression. This method of optogenetic component expression within *Tg(Pif6-EGFP-Larg)* zebrafish embryos resulted in robust and reproducible recruitment of Larg to the cell cortex throughout the embryo in response to 640nm light, while Larg was maintained in the cytoplasm in response to 730nm light (Figure 1A & B).

To test whether recruitment of Larg to the cell cortex resulted in RhoA activation, we mosaically injected *Tg(Pif6-EGFP-Larg)* embryos with mRNA encoding a RhoA biosensor, dT-2xrGBD (Mahlandt *et al*, 2021), alongside mRNA encoding PHYB-Caax, and the PCB chromophore. The dT-2xrGBD biosensor comprises the Rhotekin G protein binding domain, tagged with dimeric tomato, which was found to relocalise more efficiently than other RhoA biosensor conformations in cell culture. We found that expression of this biosensor within zebrafish embryos in combination with our optogenetic system resulted in cell and tissue abnormalities, making it unsuitable as a routine live RhoA reporter *in vivo*. However, by mosaically expressing dT-2xrGBD, we were able to determine that RhoA activity is increased by Larg recruitment to the cell cortex within zebrafish neural epithelial progenitor cells *in vivo* (Figure 1C & D).

Next we confirmed that RhoA activation via Larg recruitment to the cortex resulted in phosphorylation of non-muscle myosin II (NMYII), essential for actomyosin contractility. We mosaically injected *Tg(Pif6-EGFP-Larg)* embryos with mRNA encoding PHYB-Caax and H2B-RFP, alongside PCB. Following one minute of 640nm light exposure, embryos were fixed and stained for NMYII, phosphorylated at both Serine 19 and Threonine 18. The level of phosphorylated NMYII was significantly higher in cells with optogenetic membrane recruitment of Larg (Figure 1E-F). Together, this data demonstrates that the Phytochrome optogenetic system can be used to recruit transgenic Pif6-EGFP-Larg to cell membranes within living zebrafish embryos, and that this is sufficient to activate endogenous RhoA signalling and NMYII phosphorylation.

Inverse light patterning results in precise and reversible Larg recruitment, deep within the developing neural rod.

We next aimed to use a light-patterning approach to restrict Larg recruitment to specific regions of tissue. To do this, we built a patterned illumination system, comprising a Cairnfocal digital mirror device (DMD) system coupled to a spinning disc confocal microscope (see methods, Figure 2A), to achieve inverse patterning of activating (640nm) and deactivating (730nm) light (Figure 2B). Inverse light patterning was necessary because Phytochrome optogenetic activation is highly sensitive to a wide wavelength of light, so even blue light during EGFP imaging causes background activation in the absence of 740nm deactivation light (Buckley, 2019; Buckley *et al.*, 2016). Using this approach, we could achieve precise and reversible recruitment of Pif6-EGFP-Larg, deep within the neural rod, to specific tissue regions (Figure 2C). The membrane/cytoplasm ratio of Pif6-EGFP-Larg during 640nm and 730nm illumination were fit to non-linear models, giving time constants of 12.1s for recruitment to the cell cortex and 10.7s for de-recruitment to the cytoplasm (Figure 2D).

Whilst inverse light patterning from the DMD is focused at a specific 2D plane within the embryo, the point spread function of the activating/deactivating light is such that the illumination occurs over a 3D volume. The size of this 3D volume is dependent on the area and shape of the 2D activation region of interest (ROI) set on the DMD. To understand the extent of out of plane activation/deactivation, a simplified numerical model (based on incoherent superposition imaging modelling) was set up to predict the 3D activation/deactivation range (see methods). Away from the focal plane, both activating 640nm and deactivating 740nm light become more diffuse. The model predicts that, for an activation ROI of 33µm x 33µm, a >90% recruiting light intensity (~2.93 mW/cm^2) would extend 23µm above and below the imaging plane. Taking ~70% as the intensity threshold for 640nm recruiting light (~2.28 mW/cm2), this would reach 32µm above and below the imaging plane in an approximately hourglass shape (Figure 3Ai). The inverse 730nm light patterning (i.e. the absence of 730nm light in a 33µm x 33µm ROI) results in >70% intensity outside of an oval that reaches 32µm (Figure 3Aii). The association of PhyB and PIF6 depends on the ratio between 640nm and 730nm light which decreases away from the activation plane (Figure 3C), suggesting that weaker levels of recruitment would occur. Similar shapes of illumination were predicted for smaller ROIs (15µm x 15µm), but these had a more restricted axial extent of optogenetic activation (10µm above and below the imaging plane for >90%, and 14 µm for >70% 640nm recruiting light) (Figure 3B and E). To test the true axial extent of optogenetic activation, we assessed optogenetic activation at different axial distances from the DMD patterning plane (see methods). For an activation ROI of 33µm x 33µm at a depth of 30µm from the enveloping layer (EVL) of the embryo, weaker and broader levels of optogenetic recruitment was seen 30µm below the activation plane (Figure 3D), supporting the hourglass shape predicted from the simulation at ~70% 640nm recruiting light.

Together, this data demonstrates that the Phytochrome optogenetic system can be used to reversibly recruit Larg (and therefore to activate RhoA and phosphorylate NMYII) deep within the developing

directions during peak velocity (Figure 5J). Therefore, the small-scale nuclear displacement was propagated on a large-scale tissue distance along the AP axis.

The zebrafish hindbrain is undergoing a mesenchymal-to-epithelial transition during this developmental stage, characterised by apical-basal polarisation and a reorganisation of junctional components such as actomyosin. Whilst this would be expected to affect the mechanical properties (and therefore force propagation) at the apical-lateral junctions, we wanted to test whether force propagation at the lateral cortices was affected by the epithelial state of the tissue. We therefore restricted our ROIs to the lateral portion of cells, as above, and quantified velocity magnitude between neural keel (12ss-15ss) and neural rod stage embryos (16ss-21ss). This demonstrated that the magnitude of velocity in either the north or south region (depending on directionality of response) was similar between both stages of development (Figure 5K) and the peak velocity was not significantly different (Figure 5L). We therefore continued to pool neural keel and rod embryos for further analysis. Together, this data demonstrates first that locally activating RhoA optogenetically is an effective method to cause local tissue contractility at depth within a 3D tissue. Second, it uncovers an unexpectedly asymmetric and long-range displacement of surrounding tissue along the AP axis, that is independent of the epithelial state of the tissue.

A dynamic oscillation of expansion and contraction is present along the AP axis

To further investigate the tissue shape-change during this asymmetric displacement of the tissue, we extracted strain rate tensors from the PIV data (see methods). We first considered isotropic strain rate, which quantifies the rate of expansion and contraction of the tissue. Kymographs were generated of isotropic strain rates across an anterior-posterior column overlying the ROI in anteriorly directed embryos (Figure 6A & B). Before actomyosin activation (i.e. in a control situation), this demonstrated the presence of dynamic spatial oscillations of expansion and contraction along the anterior-posterior axis (Figure 6A, B and S3A). Upon actomyosin activation, a pronounced area of expansion was seen within the ROI (Figure 6B). Whilst we observed mediolateral shortening of cells in the ROI (Figure 4), this suggests a compensatory anterior-posterior expansion of the region. The spatial oscillation of expansion and contraction along the AP axis was maintained during activation, creating a static standing wave along the anterior-posterior axis (Figure 6A-C and S3B). During relaxation of actomyosin, the polarity of this response was reversed, with contraction seen within the ROI and expansion either side (Figure 6B). The magnitude of the isotropic strain rate was relatively low, with a mean amplitude of $1.07 \times 10^{-4} \pm 2.7 \times 10^{-5}\ s^{-1}$ or 1.69 ± 0.264 z-score (mean ± SD), which did not significantly change during activation (Figure 6H). The mean wavelength of the oscillation was 52.8 ± 2.34 µm (mean ± SD), which also did not significantly change during activation (Figure 6I). Interestingly, anterior-posterior rhombomere length is approximately 50 µm (Maves *et al*, 2002; Terriente *et al*, 2012), suggesting that segmentation of the hindbrain may control the wavelength of oscillation.

In posteriorly directed embryos, we found similar oscillations in isotropic strain rate, including expansion in the ROI during peak activation velocity (Figure S4A & C). In this case there were differences in expansion and contraction between the tissue neighbouring the ROI on the anterior and posterior sides. However, the low number of embryos in which tissue moved posteriorly makes it difficult to deduce whether this difference is representative. Together, this data suggests that there is an intrinsic oscillatory property to the tissue along the anterior-posterior axis.

Local actomyosin contractility results in asymmetric shear along the AP axis

Next, we considered anisotropic strain rates which describe the rate of shear. Kymographs of anisotropic strain rate demonstrated a pronounced region of shear within the ROI during actomyosin activation (Figure 6D-F). Similarly to velocity, the shear strain rate above baseline propagated asymmetrically in the anterior-posterior axis to at least 84 µm in the anterior (Figure 6F) and at least 66 µm in the posterior direction (Figure S4B). We found that during peak velocity, anisotropic strain

rate was greater in magnitude than isotropic strain rate, indicating that more deformation in shape than changes in area occurred (Figure 6G). Interestingly, a degree of oscillation was also seen in anisotropic strain rate during ROI contraction. Outside the ROI, areas of highest anisotropic strain rate correlated with areas of highest contraction (negative isotropic strain rate) (Figure 6G, S4C).

We next investigated what might cause the asymmetry in tissue response. First, since we had observed oscillatory isotropic strain in the tissue before optogenetic manipulation, we investigated whether the initial parameters of tissue strain influenced directionality. However, we did not find a significant difference in strain rate magnitude or in velocity direction before activation between the anteriorly or posteriorly directed embryos (Figure 7A). Previous work has shown that, during convergent extension, anterior neuroepithelial tissue migrates towards the anterior, while posterior tissue migrates towards the posterior (Bhattacharya *et al.*, 2021; Keller *et al*, 2008; Williams & Solnica-Krezel, 2020). To determine whether there was underlying bias in the tissue along the anterior-posterior axis, we next investigated whether the positioning of the region of actomyosin activation within different rhombomeres of the hindbrain influenced the directionality of tissue response. However, the position of the ROI did not influence directionality within the anterior-posterior extent of the hindbrain. For example, tissue in which ROIs were placed in posterior rhombomeres still responded towards the anterior (Figure 7B).

Lastly, we investigated whether anisotropies in tissue structure or RhoA activation in and around the region of interest influenced directionality of the tissue response. We observed a trend for tissue movement towards areas of lower nuclear density, although the differences in nuclear density between regions were not statistically significant (Figure 7C). We also found gradients in LARG recruitment (and therefore RhoA activation) along the anterior-posterior extent of the ROIs. Although there was not a significant difference between the mean gradient of anterior or posterior directed embryos with the current statistical power (Figure 7E), these correlated with direction of tissue displacement during activation; LARG recruitment was higher at the anterior side of ROIs within tissue that moved anteriorly, whilst LARG recruitment was higher at the posterior side of ROIs within tissue that moved posteriorly (Figure 7D). To test whether this gradient was due to a gradient of the anchor, PhyB-mCherry-Caax, we compared the gradient of LARG recruitment with PhyB expression before the timelapse experiment (Figure F & G). This showed that there was no correlation between LARG and membrane-anchor gradients. We therefore suggest that the AP gradients in LARG recruitment that we see are due to tissue-intrinsic anisotropies in the localisation of LARG within the tissue. For example, we have observed that, under global activating light, LARG recruitment is higher in cells undergoing mitosis and towards the middle of the neural keel and rod (Figure 7H). Similarly, levels of RhoA activation in wild type and LARG+/PCB- embryos were also higher at the midline (Figure 7I). Junctional proteins start to assemble in medial-lateral regions of the tissue from neural keel stages, initially reaching quite far along the lateral edge of cells (Symonds *et al.*, 2020). Therefore, despite the truncated LARG transgene, LARG may be preferentially recruited to forming junctions and to cells undergoing mitosis. We conclude that this introduces local gradients in LARG recruitment (and therefore to actomyosin contractility) within the ROIs, which may be sufficient to initiate a highly asymmetric tissue response.

Together, this data suggests that there is an underlying wave-like propagation of force between rhombomeres along the anterior-posterior axis, with alternating areas of expansion and contraction. When a local contractile force is introduced on the mediolateral axis, this tangentially propagates shear strain along the AP axis. Local anisotropies within the ROI and neighbouring tissue may initiate the highly asymmetric response, towards either the anterior or the posterior of the embryo.

Discussion

Optogenetic method to locally alter tissue stress deep within a living vertebrate embryo

We have used the phytochrome optogenetics system to manipulate actomyosin contractility within specific regions of tissue, deep within the developing zebrafish neural tube (Figures 1-4). The low activation intensities and long wavelengths of light required for activation and deactivation of the system resulted in no noticeable bleaching or phototoxicity over the periods of activation used in this study. Although we did not have need of a second visualisation channel for these experiments, the background deactivation 740nm light made it possible to image simultaneously in both green and red, while activating a specific ROI (Movie S1), expanding the potential for using this technique to study smaller scale processes such as neighbour exchange. Whilst the longer wavelengths and high sensitivity of the phytochrome system precluded the use of high energy variable wavelength lasers for two photon activation over predefined 3D volumes, we were able to predict the shape of 3D activation generated from 2D light patterning (Figure 3). The fast dynamics and reversibility of the phytochrome system allowed us to measure the immediate response of surrounding tissue to these local alterations in tissue stress, using PIV analysis (Figures 5 and 6). Both the optogenetic manipulation of local tissue stress and the measurement of strain rates via PIV are non-invasive. The optogenetic recruitment of LARG allows the activation of endogenous RhoA within the working range of the cells. This approach allows the *in vivo,* physiological measurement of force propagation in response to local alterations in tissue stress.

Our optogenetic approach complements other *in vivo* approaches to manipulate and measure stress and strain. For example, elegant studies using the injection of magnetically responsive oil droplets into zebrafish embryos allowed the precise measurement of anisotropic tissue stress over small distances in response to a specified change in stress, demonstrating a fluid-to-solid jamming transition at the tailbud (Mongera *et al*, 2018). This highlighted the importance of local changes in tissue stress in mediating differences in tissue fluidity and directional morphogenesis.

Long-range force propagation

While viscous neighbour exchange occurs in response to deformations at the minutes-hours timescale, the zebrafish presomitic mesoderm responds to short-scale deformations of seconds to minutes as an elastic tissue (Mongera *et al*, 2023). In line with this finding, our study in the zebrafish neuroepithelium shows an elastic reversal in tissue displacement direction following activation and deactivation of RhoA (Figure 5), by providing a measurement of the displacement of zebrafish neuroepithelial progenitor cells within seconds of a local alteration in stress. Shear strain was demonstrated to propagate over 80µm along the anterior-posterior axis (Figure 6C). Our findings directly demonstrate that local alterations in cellular strain can be rapidly propagated via lateral cell membranes across large distances, enabling coordinated morphogenesis at the tissue scale. This is relevant to understanding the role of force propagation during directional morphogenesis, such as tissue elongation via compaction (Thomson *et al*, 2021). It is also relevant to understand how forces from external tissues can impact morphogenesis. For example, opposing tissue flows in the developing anterior neural plate, established by differential connectivity to the underlying involuting mesendoderm tissue, lead to tissue folding and shaping (Inman *et al*, 2023).

An important area of future research is to understand how mechanical force is decoded by cells to reciprocally alter biochemical signalling (Kindberg *et al*, 2020). In the current study, the elastic and long-range propagation of force within the tissue suggests an active mechanical response of cells to their local deformation via their cell-cell adhesions, as predicted by micropatterning optogenetic experiments (Ruppel *et al.*, 2023). Active force propagation has been demonstrated within the *Drosophila* endoderm, in which initial Fog signalling-induced NMYII contractility is propagated as a wave through the tissue without further Fog signalling (Bailles *et al*, 2019). At the cell scale, elegant optogenetic experiments in combination with optical tweezers have demonstrated that the actin cytoskeleton is critical in propagating tensile forces around the cell cortex, and that deformation of the cell membrane alone is not sufficient for force propagation (De Belly *et al*, 2023). Therefore, in the

context of multicellular tissues, the cadherins linking actin cytoskeletons between cells likely play a critical role in facilitating active propagation of mechanical forces (Pannekoek *et al*, 2019). We found that velocity magnitude of neural keel (12ss-15ss) and neural rod stage embryos (16ss-21ss) in response to local stress alteration were comparable (Figure 5K & L), enabling us to pool results from keel and rod stage embryos. This suggests that the degree of epithelialisation does not have a significant impact on the ability of cells to propagate force via lateral adhesions. This is likely because the level of lateral cadherin-based adhesions and cellular packing remains similar over the course of mesenchymal to epithelial transition of the zebrafish neuroepithelium. Future studies should investigate how cadherin-based lateral cell-cell adhesions actively transduce and propagate forces. It would be interesting to determine whether force propagation might be altered by local differences in levels of cadherins, such as in the tailbud, which has a N-cadherin dependent gradient in yield stress, linked to the extent of extracellular spaces (Mongera *et al.*, 2018).

Asymmetric directionality of force propagation

In addition to demonstrating rapid, long-range force propagation, our study uncovered an unexpected asymmetry of response; tissue displacement occurred in either the anterior or posterior direction (Figure 5), resulting in asymmetric shear strain (Figure 6D-F). We demonstrate that small local AP gradients in nuclear density and Larg recruitment (and therefore in contractility) correlate with the directionality of tangential force propagation (Figure 7C). Although these results are not statistically significant at the current power, this suggests that small local gradients in density or actomyosin activity may initiate a highly asymmetric response across a much wider area of tissue. Density has previously been shown to be inversely proportional to velocity magnitude in expanding MDCK monolayers (Petitjean *et al*, 2010; Tlili *et al*, 2018), suggesting that in our tissue higher nuclear density may not be permissive to changes in velocity. The possibility of a large-scale asymmetric response resulting from local gradients in actomyosin activity is interesting, since a computational model of *Drosophila* germband extension only enabled tissue elongation with a graded planar polarised actomyosin (Dicko *et al.*, 2017). In the same tissue, mechanical feedback at apical-lateral junctions has also been shown to play a role in the establishment long-range NMYII gradients and tissue flow patterns (Gustafson *et al.*, 2022). If the same process of dynamic NMYII recruitment occurs in lateral membranes, this could explain how the introduction of a local gradient in lateral contractility might initiate an active and directional propagation of force propagation over long distances.

As well as gradients in contractility, another parameter that can have a profound effect on the directionality of force propagation is local anisotropies in geometry. For example, during *Drosophila* gastrulation, the anteriorly localised cephalic furrow acts as barrier for tissue deformation, therefore orienting the flow towards the posterior (Dicko *et al.*, 2017). Whilst our results suggest that rhombomere boundaries may constrain the spatial periodicity of waves of expansion and contraction, they do not prevent the propagation of force, which reaches over 80µm along the AP axis (Figure 6). Another potentially relevant geometric feature to consider is curvature, both at the tissue scale and at the scale of individual cells, since curvature is important in modifying the mechanical equilibrium across a surface (Dicko *et al.*, 2017). The developing zebrafish neuroepithelium is a curved structure, so it is possible that small differences in the placement of ROIs in relation to overall tissue curvature or local cellular curvature could introduce an imbalance in mechanical equilibrium, leading to asymmetric force propagation. As cell segmentation approaches evolve, it will be important to take into account the 3D shape of cells and tissue to interpret the role of geometry on force propagation. However, so far, the full segmentation of complex pseudostratified epithelial cells has been achieved via more manual approaches (Gomez *et al.*, 2021).

Taken together with the literature, our work suggests that a combination of local gradients in contractility and robust mechanical coupling between cells drives a far-reaching and highly directional propagation of force at the tissue level. To fully understand the mechanisms behind directional

morphogenesis and precise pattern emergence, future research should address the interrelationship between biochemical and mechanical signalling in this context. For example, during chick hindgut formation, imaging studies demonstrated that an initial FGF8 gradient caused contractility of endoderm cells, which then pulled non-contractile cells into the FGF8 region, causing them to contract (Nerurkar *et al*, 2019).

Compressional waves along the AP axis

Another unexpected finding was the presence of oscillating regions of isotropic expansion and contraction along the AP axis in the control tissue before activation. Isotropic strain rates over the AP axis before activation of RhoA (in baseline conditions) show a propagating multi-nodal spatial oscillation (Figure 6B). Upon activation of RhoA within an ROI, areas of expansion and contraction were stabilised, creating a standing wave along the AP axis with a mean wavelength of ~53µm (Figure 6A-C). Temporally oscillating stresses have previously been measured in the zebrafish hindbrain using deformable polyacrylamide beads, which were suggested to result from synchronised cell divisions (Träber *et al*, 2019). In future, it would be interesting to see how these temporal oscillations intersect with the spatial oscillations that we find at the rhombomere length scale. The emergence of such self-organising oscillations of expansion and contraction are strikingly similar in pattern to that of spatiotemporal oscillating cell movement and isotropic strain seen in confined monolayers of human keratinocytes and enterocytes (Peyret *et al*, 2019). This study revealed that the periodicity of oscillations and velocity correlation length correlated with the size of the geometrical confinement of the tissue and that cadherin-based cell-cell adhesions are critical to generate oscillatory behaviour. Such similarities in oscillatory patterns, despite the different behaviours (cell migration vs. cell deformation) and timescale (30 hours vs. a few minutes), highlight the propensity of epithelial tissue for self-organised oscillations (Balaji *et al*, 2017; Fernandez-Gonzalez & Zallen, 2011; He *et al*, 2010; Martin *et al*, 2009; Sawyer *et al*, 2011; Serra-Picamal *et al*, 2012). It also illustrates again the importance of cadherin-based adhesions in propagating force between cells, therefore enabling pattern emergence at the tissue level. Oscillatory contractions of the adherens junctions of *Drosophila* germband cells were found to cause cell shape extension along the AP axis, required for axis extension (Sawyer *et al.*, 2011). Our results suggest that oscillations between lateral cell edges may also be important in mediating force propagation.

Surprisingly, we found that, whilst isotropic strain rate wave becomes static during activation, the wavelength of isotropic strain rate across the anterior-posterior axis is sustained (Figure 6I), appearing to be an inherent property of the tissue. This suggests that the spatial periodicity of oscillations may be controlled by the mechanical environment, such as geometrical confinement (Peyret *et al.*, 2019). Geometrical constraints in our tissue could include the basal edges of the neural tube and segments such as the rhombomeres, of which the latter has an approximate 50µm AP length (Maves *et al.*, 2002; Terriente *et al.*, 2012). This matches the wavelength in isotropic strain. Therefore, it is possible that the spatial periodicity is controlled by rhombomeres, or that the natural frequency of the tissue instructs rhombomere size. This presents an area of future study. We hypothesise that the spatial oscillations in expansion and contraction that we see along the AP axis may be involved in directionally propagating force between rhombomeres along the AP axis.

Conclusions

We have demonstrated that optogenetic activation of RhoA signalling leads to phosphorylation of NMYII and rapid contraction of the actomyosin cytoskeleton within zebrafish neuroepithelial progenitor cells, *in vivo*. Inverse light patterning of recruiting and derecruiting light in a 2D plane results in a predictable 3D recruitment ROI deep within the developing neural tube. This technique is adaptable to a wide range of research questions, since it allows the behaviour of cells and tissue to be quantified before, during and after a precise and reversible manipulation in actomyosin contractility, deep within the developing zebrafish embryo. The ubiquitous promoter within the transgenic line

drives expression of Larg in all tissues. Particle image velocimetry demonstrated an underlying wave-like propagation of forces between rhombomeres along the anterior-posterior axis, with oscillations between tissue expansion and contraction matching rhombomere length. Local changes in tissue contraction in the mediolateral axis of neuroepithelial progenitor cells led to rapid tangential shear deformation of the tissue along the anterior posterior axis. This force propagation was long ranging, suggesting the active mechanical propagation of cell generated force. The response did not depend on the level of epithelialisation of the tissue, and propagated asymmetrically through the anterior-posterior axis, possibly in response to local AP gradients in nuclear density or Larg recruitment. This helps to explain how precise morphogenetic patterns can occur across distance in response to relatively small local anisotropies in cellular contractility. Further investigations into the molecular mechanisms of force transmission via cadherin-based cell-cell adhesions will be important to further understanding of how such anisotropies might arise. Together, the ability to precisely and reversibly manipulate actomyosin contractility at depth within a physiological *in vivo* vertebrate system has uncovered rapid, long-range and directional mechanical communication between cells.

Methods

Experimental design

All procedures were carried out with Home Office approval and were subject to the University of Cambridge and the University of Manchester AWERB Ethical Committee review (PPL PF2F15847 and 4544659). Experiments were designed according to ARRIVE guidelines (https://arriveguidelines.org/arrive-guidelines). Since the experimental units were either individual cells or regionally specific areas of tissue, internal controls were used; e.g. a non-optogenetic region of tissue or a region of tissue before optogenetic activation. Sample sizes are included in figure legends. Only embryos that were morphologically normal were included in the study. It is not possible to select for gender, so a random mixture of males and females were used. Blinding was not relevant to these experiments. However, embryos were selected in an unbiased way, based on their Z-score (see below). PIV data was then automatically generated from standardised regions of interest, as described in the figure legends. Outcome measures are described in the figures and legends. Statistics, details of transgenic animals and experimental procedures are detailed below and in supplementary methods. Results are reported with variance and statistical outcomes, as detailed in figures and legends.

Transgenic line details

Tg(ubb:Ath.Pif6-EGFP-arhgef12a) fish express the first 100 amino acids of Arabidopsis PIF6 (Gene ID: 825382), codon optimised for mammalian expression, as previously published (Buckley *et al.*, 2016). This is fused with EGFP and the majority of the DH domain from zebrafish Arhgef12a (Gene ID: 562455). The fusion protein is expressed under the ubiquitin B promoter, which drives transcription in all tissues. See supplementary methods.

Patterned illumination system

The Cairnfocal is a commercial system designed and developed by Cairn research (Martin Thomas 2014, Two mirror optical arrangement for digital micromirror device, patent EP2876479B1), with minor custom modifications (as detailed below). The system is composed of a digital mirror device (DMD), two light sources, two sets of Offner triplets and a plurality of individually adjustable mirrors. The layout of this system allows two light sources to be simultaneously patterned by the DMD. To achieve inverse conformation of activating (640 nm) and deactivating (730 nm) light onto the tissue, a LDI-7 Laser Diode Illuminator (89 North) and a 730 nm LED (Thorlabs M730L5) are positioned on the left and right beam path. The light from each source is collimated and projected to the Offner triplet. Both sets of Offner triplets are identical and focus the incoming light on the DMD at the incident angle of positive 12-degree and negative 12-degree.

The DMD used in the system is ViALUX WUXGA 0.96" Type A. The DMD is positioned at the relayed image plane which is centred on the optical axis of the light path to the microscope. Each micro-mirror on the DMD flips to the “on” or “off” position with respect to the input pattern to reflect the light from either source. The patterned beam is re-collimated, folded and projected to the back port of a Nikon Ti2 inverted microscope to activate/deactivate specific areas of the specimen. A shortpass dichroic filter (T610SPxxr, Chroma) is used in the fluorescent turret of the microscope frame to direct the light to the sample. At the sample plane for activation, 1% 640 nm laser power (3.25 mW/cm^2) and 100% 730 nm LED power (293 mW/cm^2) were used for patterning experiments. The DMD was controlled using python scripts called through MetaMorph Journals.

Confocal Unit

The imaging part of the photomanipulation system is built around a Nikon Ti2 inverted microscope with incubation system and a commercial disc confocal system (CrestOptics X-light V3). The confocal system is composed of an LDI-7 Laser Diode Illuminator (89 North), a lenslet array, a moveable spinning disk, two cameras (Photometrics Prime 95B), filters and lenses. The excitation light from the Laser illuminator is cleaned by an excitation filter (Chroma ZET405/470/555/640x). Then the light is focused on the spinning disk (CrestOptics, SP 50 µm/400 µm pinhole), passing through the pin holes, reflected by a dichroic mirror (Chroma ZT405/470/555/640rpc-UF2), and refocused on the microscope imaging plane. The emission light from the specimen is collected by the same objective, following the same beam path to the spinning disk, cleaned by an emission filter, (Chroma ZET405/470/555/640m-OD8), and projected to the camera. The emission light can be split into 2 channels with a dichroic mirror (Chroma T565lpxr-UF2). A matching bandpass filter is placed in front of each camera to limit the detected spectral range and block unwanted stray lights (Chroma ET525/50m and ET605/70m). The typical excitation power density at the sample plane for imaging were around 6 mW/cm^2 for the 470 nm laser (at 25%) and 0.4 mW/cm^2 for the 555 nm laser (at 1%). A collimated 730 nm LED (Thorlabs M730L5) was mounted within the incubation system, optogenetic deactivation of the whole imaging dish between experiments. For all imaging, a 40x NA 1.25 Silicone objective (Nikon CFI Plan Apochromat Lambda S 40XC Sil) was used.

Optogenetic imaging

Embryos were cultured at 24-28.5˚C, to achieve the desired stage of development. Following injection with mRNA and PCB, embryos were kept in the dark and mounted under 730-740nm light using mounted and diascopic light sources (Thorlabs, M730L5, and Zeiss, KL1500 LCD fitted with a 740nm band-pass filter (Envin Scientific), respectively). Embryos were mounted in 1-1.5% agarose diluted in E3 medium. The stage positions of embryos mounted on the light patterning microscope were found under 730 nm LED light, to prevent activation of RhoA by background light. The field of view was positioned at 30µm below the enveloping layer and centred over rhombomere 5 of the hindbrain, using the otic vesicle as a landmark. Single dual colour images following 1 minute of global 630nm and 730nm illumination were taken before experiments to verify successful optogenetic recruitment and derecruitment. Embryos were exposed to 2 minutes of global 730nm illumination prior to experiments to ensure experiments began from a deactivated state. For optogenetic timelapse experiments, images were taken every 5 seconds, using 1 second exposure, concurrent with constant light patterning (see Figure S5A). To estimate the level of activation in the z-axis, a 33x33 µm ROI was activated within the neural tissue 30µm beneath the enveloping layer for 2 minutes. Snapshots were the taken at different axial distances from the ROI plane. To ensure that imaging did not cause background optogenetic activation, each snapshot was interspersed with another 2 minutes of light patterning (see Figure S5B). Experimental photoactivation and imaging pipelines were operated using MetaMorph journals.

3D activation simulation (incoherent superposition imaging modelling):

To simulate the intensity distribution of the activation and deactivation light around the imaging plane a model based on diffraction-limited imaging theory is used, implemented in MATLAB based on code

from Voelz, 2011. An aberration free incoherent superposition imaging model simulates the intensity distribution after propagating through the objective lens at multiple distances from the objective (Voelz, 2011). The objective is set to a 40x silicone oil immersion objective with an NA of 1.25. The image size is set to 330 x 330 µm (1200 x 1200 pixels) to match experimental conditions. The simulations were run for 640 nm light (activation) 730 nm light (deactivation). Light reflected from the active pixels of the DMD to the objective is assumed to be perfectly collimated and focussing on the ideal imaging plane. The region of interest for activating is either set to the 15µm x 15µm or 33µm x 33µm on the imaging plane. The overall propagation range is +/-50 µm in steps of 5µm. The maximum intensity of the activation light is normalised to 1 and used to reconstruct the 3D volume.

Particle Image Velocimetry

Tissue velocity was quantified through particle image velocimetry (PIV) by cross-correlating successive image pairs.

Before analysis, images were manually screened for high specificity of recruitment in the ROI. Images converted to 8-bit and horizontally flipped or rotated in Fiji to ensure ROIs were on the left side and the anterior-posterior axis was aligned along the y-axis. Each image underwent preprocessing, specifically noise reduction with a 5x5 pixel wiener filter (wiener2 of the Image Processing Toolbox, MATLAB) and a running average of the previous and following frames using a custom MATLAB script.

For PIV analysis, we used PIVLab v2.56 for MATLAB, implementing an initial 64×64 pixel interrogation window and secondary 32×32 pixel window at 50% overlap (equivalent to 17.6x17.6 µm and 8.8x8.8 µm respectively), which are in the order of the size of a cell. Resulting velocity fields were smoothed with a 5x5 µm spatial filter before quantification and further analysis.

Strain Rates

Strain rates characterize local tissue deformation kinetics. They can be decomposed into isotropic and anisotropic components (Serrano Najera & Weijer, 2020). The strain rates can be derived from the gradient of the velocity *v* obtained from PIV. ∇*v* can be decomposed into a symmetric part (strain rate tensor, ξ) and an anti-symmetric part (spin tensor, ω):

$$\nabla v = \xi + \omega$$

Where:

$$\xi = \frac{\nabla v + \nabla v^{T}}{2}; \ \omega = \frac{\nabla v - \nabla v^{T}}{2}$$

Expanding the strain rate tensor ξ:

$$\xi = \begin{pmatrix} \frac{\partial vx}{\partial x} & \frac{1}{2}\left(\frac{\partial vx}{\partial y} + \frac{\partial vy}{\partial x}\right) \\ \frac{1}{2}\left(\frac{\partial vx}{\partial y} + \frac{\partial vy}{\partial x}\right) & \frac{\partial vx}{\partial y} \end{pmatrix}$$

ξ can be further decomposed into an Isotropic Term (ξ_{iso}) with the form of a scalar times the Identity, or unit tensor (I), plus an Anisotropic Term (ξ_{ani}) with the form of a traceless symmetric tensor.

$$\xi = \xi iso + \xi ani$$

Where:

$$\xi iso = \frac{1}{2}\begin{pmatrix} \frac{\partial vx}{\partial x} + \frac{\partial vx}{\partial y} & 0 \\ 0 & \frac{\partial vx}{\partial x} + \frac{\partial vx}{\partial y} \end{pmatrix}; \xi ani = \frac{1}{2}\begin{pmatrix} \frac{\partial vx}{\partial x} - \frac{\partial vx}{\partial y}, & \frac{\partial vx}{\partial y} + \frac{\partial vy}{\partial x} \\ \frac{\partial vx}{\partial y} + \frac{\partial vy}{\partial x}, & \frac{\partial vx}{\partial x} - \frac{\partial vx}{\partial y} \end{pmatrix}$$

The eigenvalue of isotropic strain rate tensor (ξiso) describes the magnitude of local expansion or contraction rate equally in both axes. The anisotropic strain rate tensor (ξani) represents the shear strain rate. It possesses two eigenvalues of equal magnitude and opposite sign. The eigenvector paired with the negative eigenvalue defines the axis of contraction. Orthogonally, the positive eigenvalue eigenvector outlines the axis of expansion.

Analysis of velocity and strain rates

To analyse tissue movements surrounding optogenetic activation, images were subdivided into a grid with unit areas matching the illumination area. One grid unit was centred on the region of interest. The grid units adjacent to the ROI were analysed and referred to as north (anterior), south (posterior) and east (medial) regions (Figure 5E). Lateral regions were excluded as the ROI was placed towards the lateral edge of the tissue. For each region, we extracted the average and standard deviation for velocity magnitude, velocity direction and strain rate eigenvalues using a custom MATLAB script. To determine the direction of response, we calculated the average circular mean of velocity direction of the combined north, south and medial regions, with mean direction above the equator being categorised as anterior and below the equator as posterior.

To enable comparison of different embryos, we standardised the parameters extracted from the PIV analysis by calculating z-scores. This indicates how many standard deviations the value is from the pre-activation mean. To determine whether embryos showed a significant increase in tissue movement, we looked at the peak velocity z-score during RhoA activation in the corresponding region to their categorised direction, for example north for anteriorly-directed embryos and south for posteriorly-directed embryos. 9 out of 12 neural keel to neural rod stage embryos analysed had a statistically significant increase in velocity of adjacent tissue during local RhoA activation (z-score above 2). This was then used as a threshold to filter embryos for further analysis.

Additionally, an anteroposterior column encompassing the width of the ROI was evaluated. Each parameter was averaged across the column width for discrete positions along the embryo anteroposterior axis, using a custom MATLAB script. To analyse the oscillation in isotropic strain rate, data was smoothed with a Savitzky-Golay filter to enable identification of peaks. Peak location was then used to calculate amplitude and wavelength from the raw data.

In summary, quantification focused on local regions immediately surrounding and along the axis of optogenetic activation, providing critical insight into light-induced tissue deformations and movements. Partitioning into discrete grid areas and columnar analysis facilitated quantitative characterization of propagation effects.

Nuclear Displacement

To quantify nuclear displacement during activation, difference between the centroids of nuclei in the north or south regions were calculated for the timepoint 60s before activation and immediately before activation, immediately before activation and 60s after activation, and immediately before deactivation and 60s after deactivation.

Statistical analysis
Statistical analysis was carried out in R Studio using R version 4.3.2. Standard statistical analyses were carried out using the rstatix package, and circular statistics using the circular package. We performed Shapiro-Wilk tests for normality and Levene's tests for equality of variance before selecting the appropriate statistical tests. Details of specific hypothesis tests are described in the figure legends.

Data and resource availability
All data and resources will be made freely available after publication. Custom MATLAB and R scripts will be found at https://github.com/Buckley-Lab-opto/Crellin-et-al-2024/. *Tg(ubb:Ath.Pif6-EGFP-arhgef12a)* fish will be available from eZIRC. Plasmids created in this study will be deposited in Addgene. Image data will be deposited in BioImage archive. For the purpose of open access, the authors have applied a Creative Commons Attribution (CC BY) licence to any Author Accepted Manuscript version arising.

Acknowledgements
Thank you to Sarah Williams for lab management, and cloning and genotyping of the *Tg(ubb:Ath.Pif6-EGFP-arhgef12a)* fish. Thank you to Kasia Anton, for her help in cloning the zebrafish specific gene for LARG and to Masa Tada for giving us a plasmid containing the *ubb* backbone. Thank you to the Cambridge Advanced Imaging Centre for help and access to confocal microscopy and to Cairn research for help in building the light patterning system. Thank you to Cambridge University Biomedical Services for looking after zebrafish stocks.

Competing interests
The authors declare no competing or financial interests.

Author Contributions
HAC: Investigation and data curation (optogenetics imaging experiments), methodology (setting up optogenetics pipeline), formal analysis and visualisation (writing R-code, PIV analysis, designing analysis methods and visualisations, making figures), writing – writing, review and editing.
CZ: Investigation and methodology (building the light patterning system, writing code to run the experiments), formal analysis & visualisation (figure 3).
GSN: Investigation, formal analysis, visualisation & methodology (writing Matlab code, PIV analysis and designing analysis methods and visualisations).
AR: Investigation & formal analysis for Figure 1E&F.
KO'H: Funding acquisition, resources, supervision, methodology (building the light patterning system, setting up optogenetics pipeline)
MOL: Supervision, resources, methodology (building the light patterning system)
CEB: Conceptualisation, funding acquisition, resources, supervision, investigation & data curation (optogenetics imaging experiments), methodology (setting up optogenetics pipeline), writing – original draft, writing – review and editing.

Funding
This research was financially supported by: **CEB**—the Wellcome Trust and Royal Society (Sir Henry Dale Fellowship grant no. 208758/Z/17/Z and Dorothy Hodgkin Fellowship grant no. DH160086), **HAC** - Medical Research Council grant no. MR N013433-1, **GSN** – Leverhulme Trust Early Career Fellowship grant no. ECF-2022-474. **CAIC** – Wellcome Trust Technology Development Grant 212936/Z/18/Z.

Figure Legends

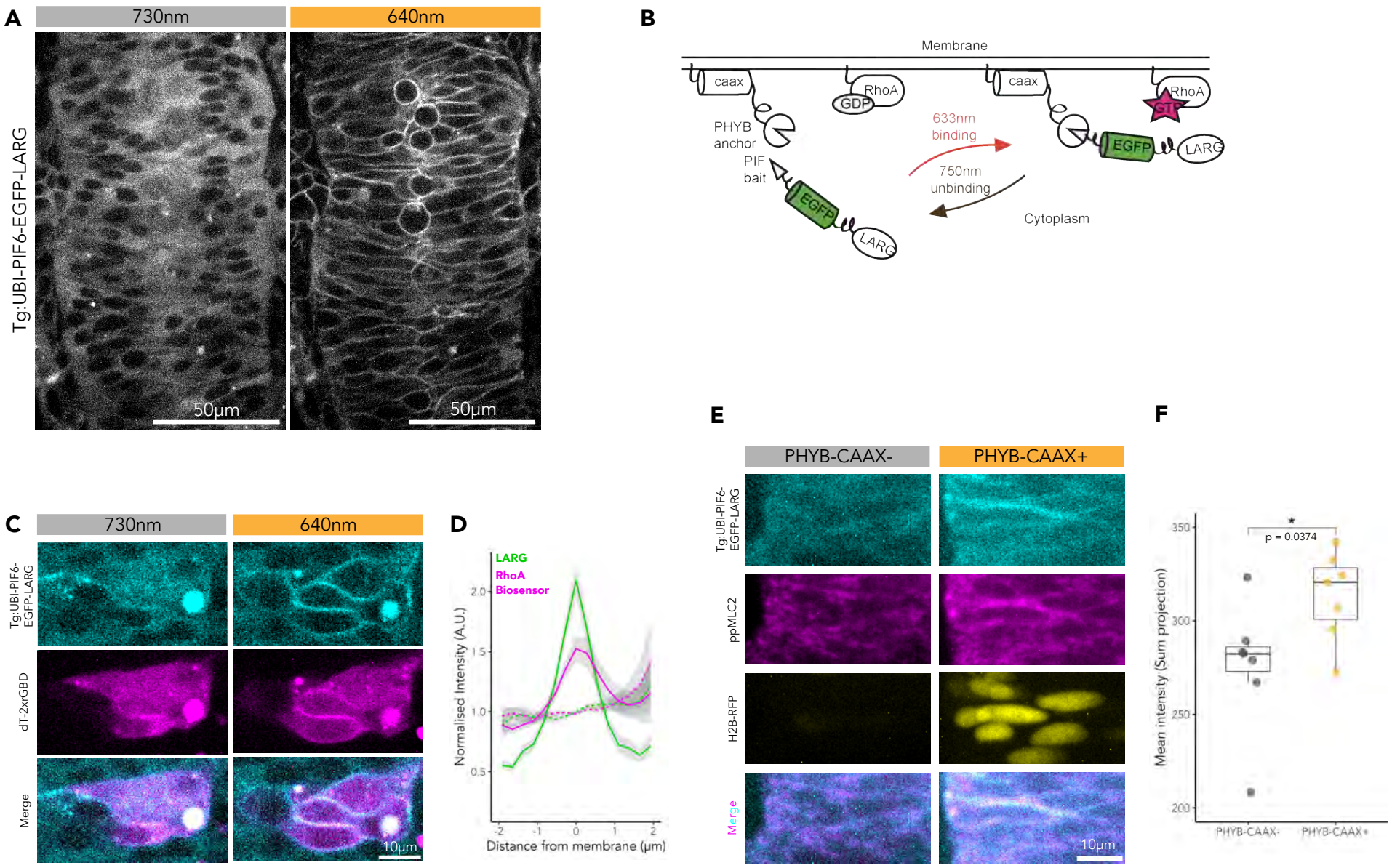
A
730nm
640nm
Tg:UBI-PIF6-EGFP-LARG
50µm
50µm
B
Membrane
caax
RhoA
GDP
caax
RhoA
GTP
PHYB
anchor
PIF
bait
633nm
binding
750nm
unbinding
EGFP
LARG
EGFP
LARG
Cytoplasm
C
730nm
640nm
Tg:UBI-PIF6-EGFP-LARG
dT-2xrGBD
Merge
10µm
D
LARG
RhoA
Biosensor
Normalised Intensity (A.U.)
Distance from membrane (µm)
E
PHYB-CAAX-
PHYB-CAAX+
Tg:UBI-PIF6-EGFP-LARG
ppMLC2
H2B-RFP
Merge
10µm
F
p = 0.0374
Mean intensity (Sum projection)
PHYB-CAAX-
PHYB-CAAX+

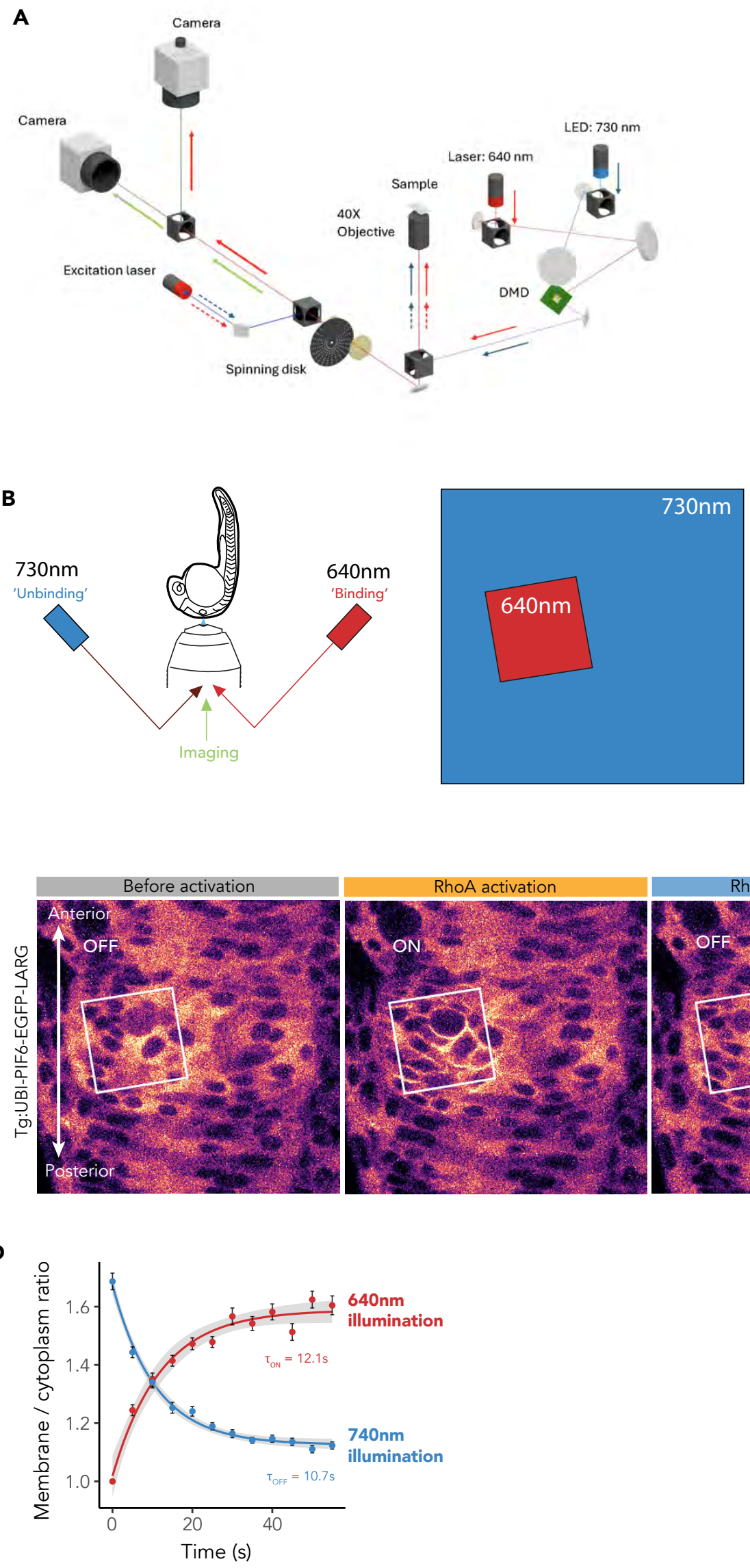
A
Camera
Camera
LED: 730 nm
Laser: 640 nm
Sample
40X
Objective
Excitation laser
DMD
Spinning disk
B
730nm
'Unbinding'
640nm
'Binding'
Imaging
730nm
640nm
C
Before activation
RhoA activation
RhoA deactivation
Anterior
OFF
ON
OFF
Posterior
20μm
Tg:UBI-PIF6-EGFP-LARG
D
Membrane / cytoplasm ratio
1.6
1.4
1.2
1.0
0
20
40
Time (s)
640nm
illumination
τ_{ON} = 12.1s
740nm
illumination
τ_{OFF} = 10.7s

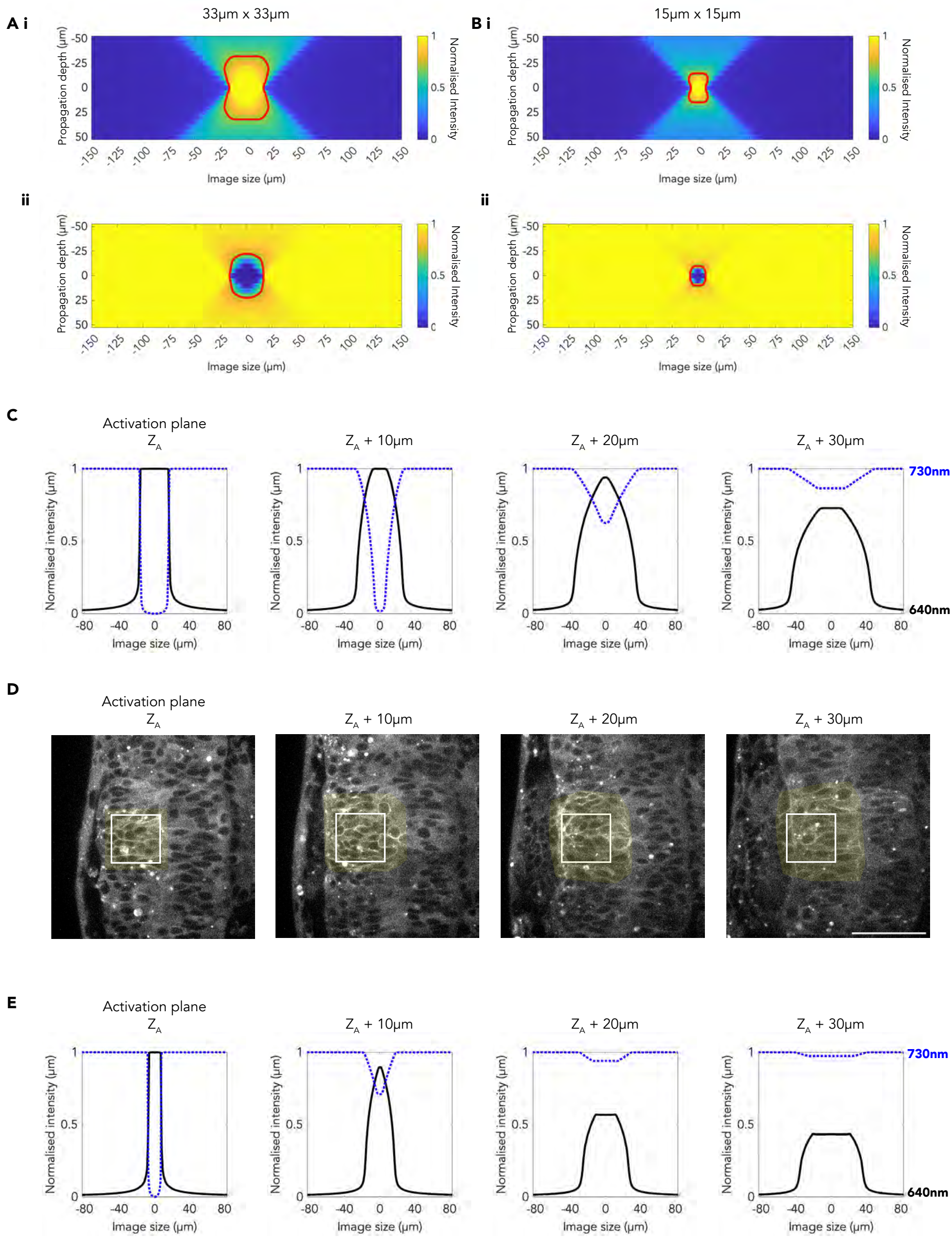
A i
33µm x 33µm
B i
15µm x 15µm
ii
Propagation depth (µm)
Image size (µm)
Normalised Intensity
C
Activation plane
Z_A
Z_A + 10µm
Z_A + 20µm
Z_A + 30µm
Normalised intensity (µm)
730nm
640nm
D
E

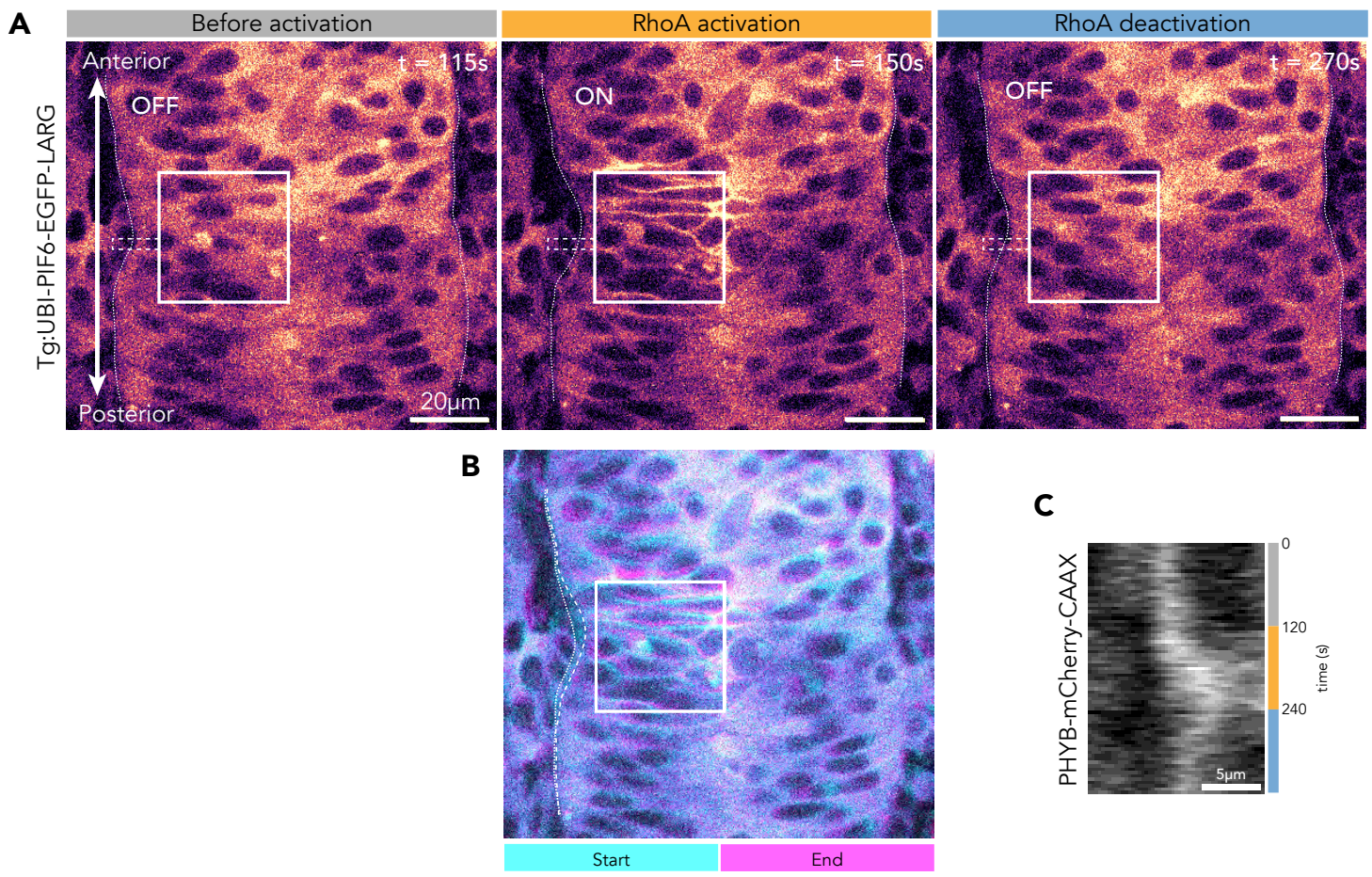
A
Before activation
RhoA activation
RhoA deactivation
Tg:UBI-PIF6-EGFP-LARG
Anterior
Posterior
OFF
ON
OFF
t = 115s
t = 150s
t = 270s
20μm
B
Start
End
C
PHYB-mCherry-CAAX
0
120
240
time (s)
5μm

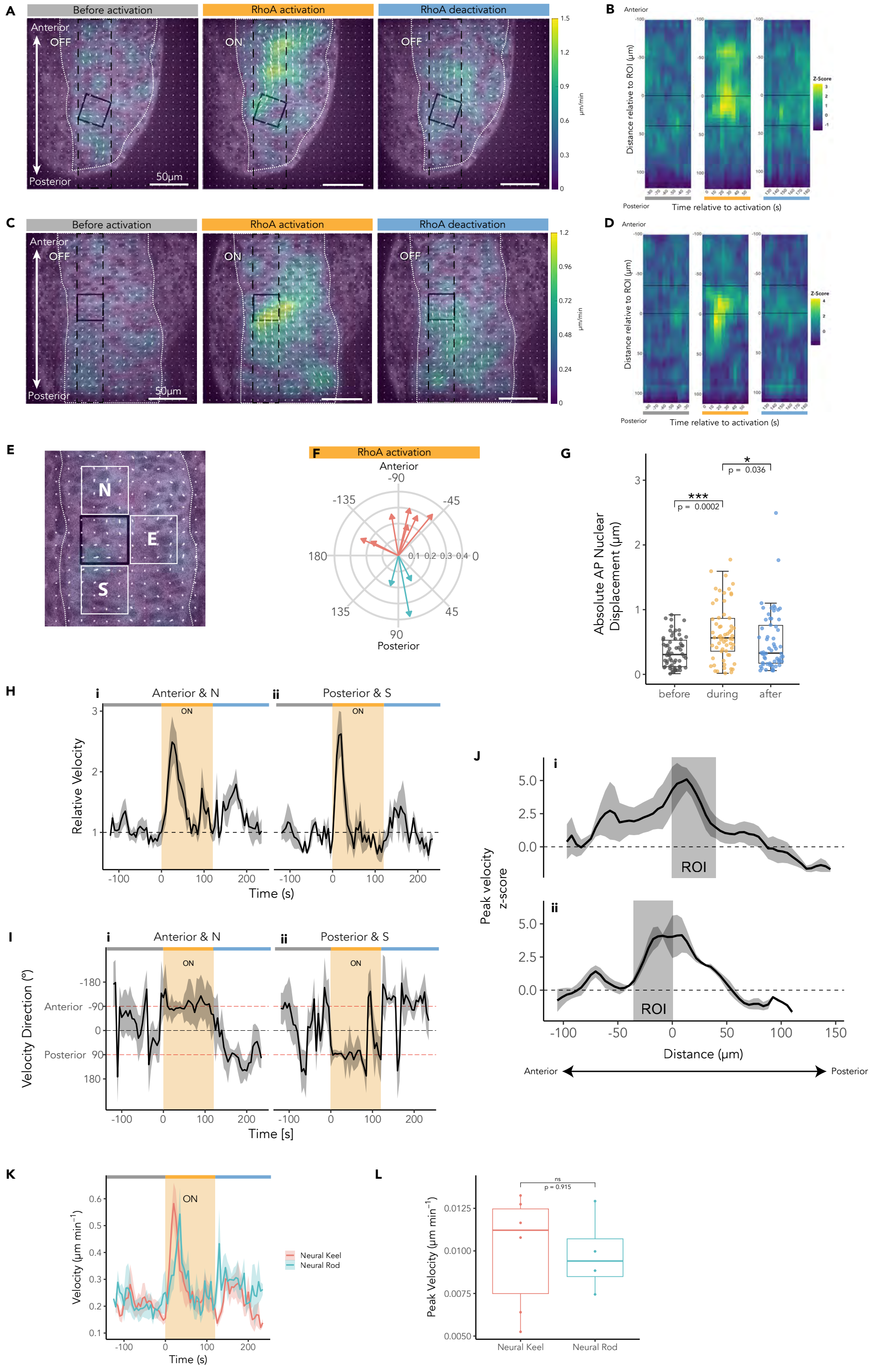
A
Before activation
RhoA activation
RhoA deactivation
Anterior
OFF
ON
OFF
Posterior
50µm
µm/min
B
Anterior
Distance relative to ROI (µm)
Z-Score
Posterior
Time relative to activation (s)
C
Before activation
RhoA activation
RhoA deactivation
Anterior
OFF
ON
OFF
Posterior
50µm
µm/min
D
Anterior
Distance relative to ROI (µm)
Z-Score
Posterior
Time relative to activation (s)
E
N
E
S
F
RhoA activation
Anterior
-90
-135
-45
180
0
135
45
90
Posterior
G
Absolute AP Nuclear Displacement (µm)
p = 0.0002
p = 0.036
before
during
after
H
i
Anterior & N
ii
Posterior & S
ON
Relative Velocity
Time (s)
I
i
Anterior & N
ii
Posterior & S
ON
Velocity Direction (°)
Anterior
Posterior
Time [s]
J
i
ii
Peak velocity z-score
ROI
Distance (µm)
Anterior
Posterior
K
ON
Velocity (µm min⁻¹)
Neural Keel
Neural Rod
Time (s)
L
ns
p = 0.915
Peak Velocity (µm min⁻¹)
Neural Keel
Neural Rod

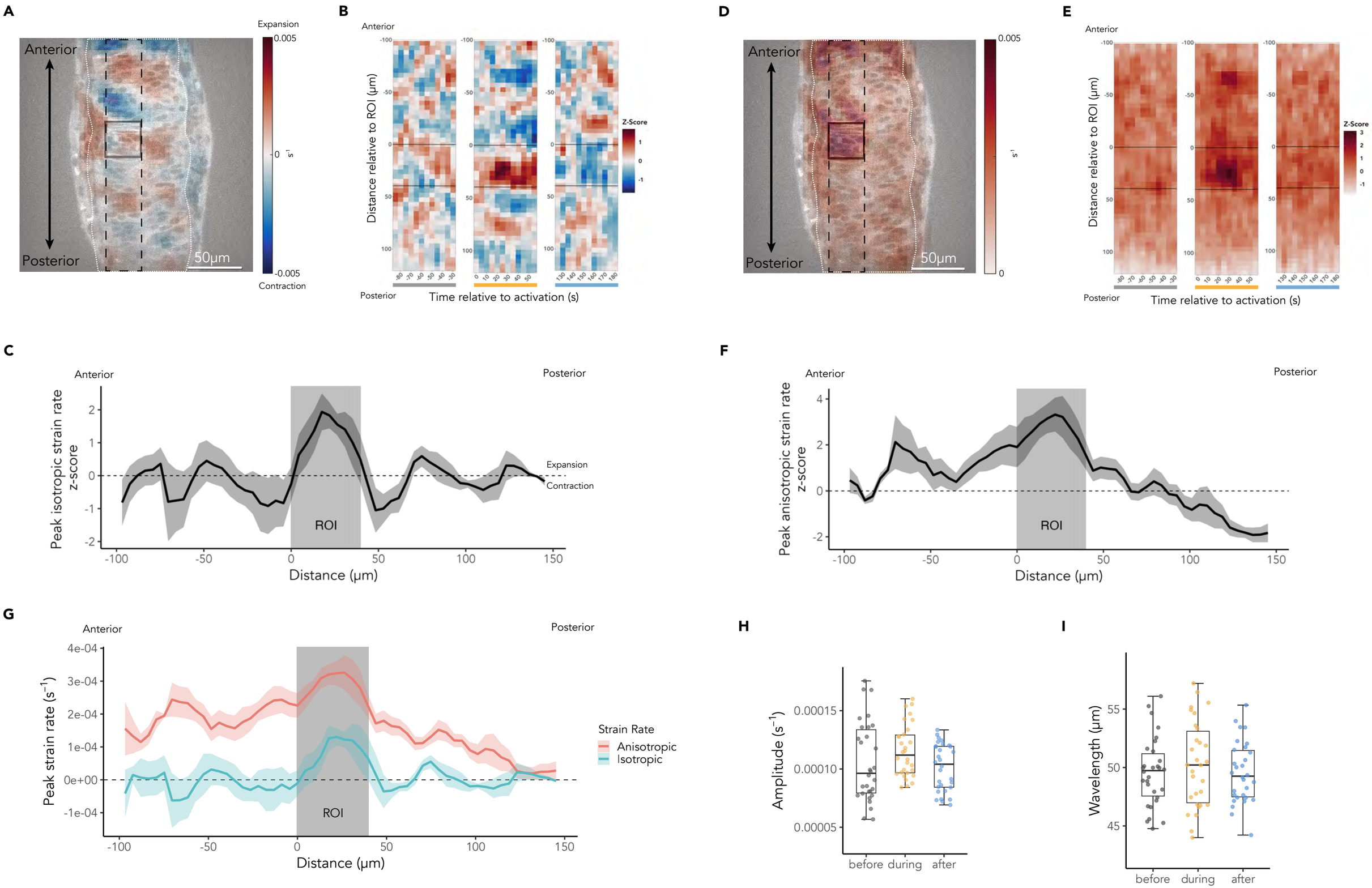
A
Anterior
Posterior
50μm
Expansion
0.005
0
-0.005
Contraction
B
Anterior
Posterior
Distance relative to ROI (μm)
Time relative to activation (s)
Z-Score
D
Anterior
Posterior
50μm
0.005
0
E
Anterior
Posterior
Distance relative to ROI (μm)
Time relative to activation (s)
Z-Score
C
Anterior
Posterior
Peak isotropic strain rate z-score
Distance (μm)
ROI
Expansion
Contraction
F
Anterior
Posterior
Peak anisotropic strain rate z-score
Distance (μm)
ROI
G
Anterior
Posterior
Peak strain rate (s⁻¹)
Distance (μm)
ROI
Strain Rate
Anisotropic
Isotropic
H
Amplitude (s⁻¹)
before during after
I
Wavelength (μm)
before during after

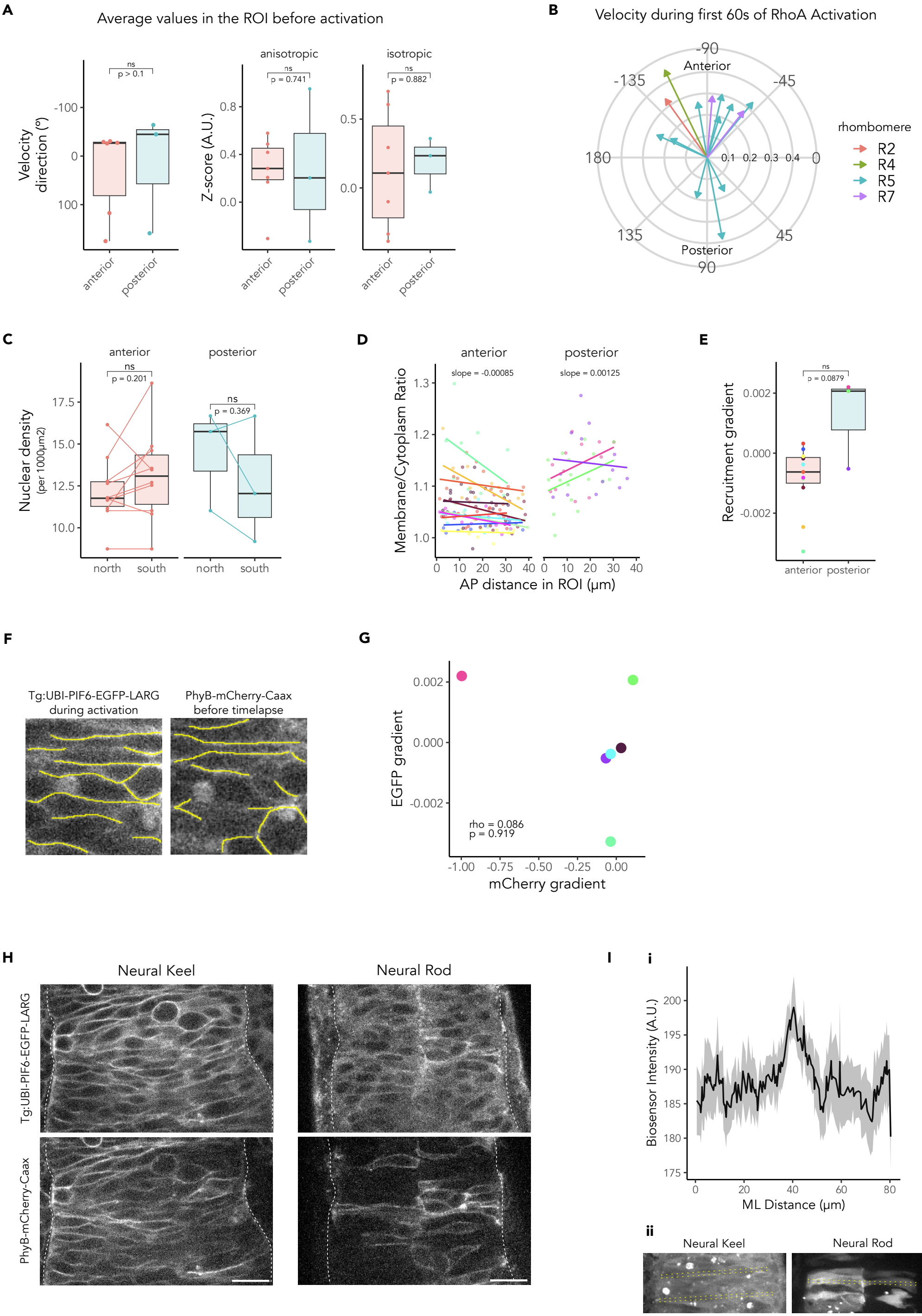
A
Average values in the ROI before activation
Velocity direction (°)
ns
p > 0.1
anisotropic
ns
p = 0.741
Z-score (A.U.)
isotropic
ns
p = 0.882
anterior
posterior
B
Velocity during first 60s of RhoA Activation
Anterior
Posterior
rhombomere
R2
R4
R5
R7
C
anterior
posterior
Nuclear density
(per 1000µm2)
ns
p = 0.201
ns
p = 0.369
north
south
D
anterior
posterior
Membrane/Cytoplasm Ratio
slope = -0.00085
slope = 0.00125
AP distance in ROI (µm)
E
Recruitment gradient
ns
p = 0.0879
anterior
posterior
F
Tg:UBI-PIF6-EGFP-LARG
during activation
PhyB-mCherry-Caax
before timelapse
G
EGFP gradient
rho = 0.086
p = 0.919
mCherry gradient
H
Neural Keel
Neural Rod
Tg:UBI-PIF6-EGFP-LARG
PhyB-mCherry-Caax
I
i
Biosensor Intensity (A.U.)
ML Distance (µm)
ii
Neural Keel
Neural Rod

Figure 1: Optogenetic LARG membrane recruitment results in RhoA activation and MLC2 phosphorylation in zebrafish neuroepithelial cells

A. Representative image showing PIF6-EGFP-LARG recruitment to the cell cortex of neuroepithelial cells in 18 somite stage zebrafish neural rod upon 730nm and 640nm illumination. Scale bar 50µm.
B. Cartoon of phytochrome optogenetic system for RhoA activation
C. Representative images showing dimericTomato-2xrGBD RhoA biosensor (magenta) and PIF6-EGFP-LARG (cyan) recruitment upon 730nm and 640nm illumination, indicating activation of RhoA under 640nm illumination. Scale bar 10µm
D. Average line profiles of PIF6-EGFP-LARG (green) and dimericTomato-2xrGBD (magenta) across cell-cell interfaces upon 730nm (dotted) and 640nm (solid) illumination, normalised to the membrane intensity during 730nm illumination. Graph shows mean and SEM. N = 59 cell-cell interfaces from 5 embryos from 3 experiments
E. Representative maximum intensity projections showing doubly phosphorylated MLC2 (ppMLC2, magenta) upregulation and PIF6-EGFP-LARG (cyan) recruitment in a PhyB-CAAX positive ROI (marked by H2B-RFP positive nuclei (yellow)), and lack of ppMLC2 and PIF6-EGFP-LARG recruitment in a PhyB-CAAX negative adjacent ROI after 640nm illumination. Scale bar 10µm.
F. Mean intensity of ppMLC2 after 640nm illumination in PhyB-CAAX positive (yellow) and negative (grey) ROIs. N = 7 PhyB-CAAX positive ROI and 7 PhyB-CAAX negative ROIs in 2 embryos from 1 experiment. Mean intensity was significantly different between groups using two-sample t-test ($t(12) = 2.34$, $*p = 0.0374$).

Figure 2:
Patterned illumination by DMD results in highly spatiotemporally specific LARG recruitment and derecruitment

A. Simplified schematic of the patterned illumination system and the spinning disk confocal microscope. The patterned illumination system is built around a DMD and two light sources (640 nm CW laser and 730 nm LED).
B. Diagram of patterned light illumination, 640nm in red, 730nm in blue.
C. Representative images showing specificity of recruitment of PIF6-EGFP-LARG to the membrane in the region of activation (ROI, white box). Images were taken at 30µm depth from the enveloping layer, in the neural keel tissue of a 15 somite stage embryo. Scale bar 20µm.
D. PIF6-EGFP-LARG membrane/cytoplasmic intensity over time following 640nm and 730nm illumination in the ROI. Ratios were normalised to levels at t = 0s of 640nm illumination. Data points are mean ± SEM of N = 10 embryos, curves are fits to non-linear models of exponential association and dissociation with the ribbon showing the 95% CI, $y = 1.018 + (1.588 - 1.018) * (1 - e^{(-0.083 * x)})$ and $y = 1.126 + (1.673 - 1.126) * e^{(-0.093 * x)}$ for 640nm and 740nm illumination respectively. The rate constants are -0.083 and -0.093 for 640nm and 740nm illumination respectively. Time constants (τ) are the inverse of the rate constant and indicate the time taken for the membrane/cytoplasmic intensity to increase by a factor of $1 - 1/e$ in the case of 640nm illumination, or decrease by a factor of $1/e$ in the case of 730nm illumination.

Figure 3:
2D light patterning using DMD results in 3D recruitment

A. Simulated cross section (xz) of the 640nm activation (i) and 730nm deactivation (ii) illumination intensity resulting from a 33µm x 33µm ROI. Red line indicates 70% intensity.
B. Simulated cross section (xz) of the 640nm activation (i) and 730nm deactivation (ii) illumination intensity resulting from a 15µm x 15µm ROI. Red line indicates 70% intensity.

C. Intensity line profile of simulated activation/deactivation light at activation plane and at 10µm intervals away from the activation plane from a 33µm x 33µm ROI.
D. Experimental data demonstrates that activation from a 33µm x 33µm ROI reaches ~30µm deeper than the imaging plane, with an increasingly broader and weaker region of recruitment (yellow overlay), in line with simulated ~70% 640nm light. Scale bar 50µm.
E. Intensity line profile of simulated activation/deactivation light at activation plane and at 10µm intervals away from the activation plane for a 15µm x 15µm ROI.

Figure 4:
RhoA activation induces local tissue deformation

A. Representative images showing reversible deformation of the basal edge of the tissue following RhoA activation in an 18 somite stage embryo. Solid white box indicates ROI. Dotted line indicates basal edge of the tissue. Dashed box indicates region taken for kymograph in C. Scale bar 20µm. See movie 1.
B. Temporal-colour coded image showing changes in cell shape from 100s of activation. Start (cyan) is t = 20s after activation and end (magenta) is t = 120s after activation. Dotted line indicates basal edge of tissue at start and dashed line indicates basal edge of tissue at end.
C. Kymograph of the dashed region in A showing the deformation of the basal edge of the tissue.

Figure 5:
Local RhoA activation induces a long-range, asymmetric tissue displacement

A. Velocity vector field of an anteriorly directed 15 somite stage embryo before activation, during peak activation and after activation. See Movie 2.
B. Space-time heatmaps of velocity z-score (average of anteriorly directed embryos, n = 7). Each panel represents an anterior-posterior column (see black dashed line of A) overlying the area of activation (ROI, solid black lines) and covers a 55s period, either before activation, immediately upon RhoA activation and immediately post activation.
C. Velocity vector field of a posteriorly directed 14 somite stage embryo before activation, during peak activation and after activation. See Movie 3.
D. Space-time heatmaps of velocity z-score (average of posteriorly directed embryos, n = 3). Each panel represents an anterior-posterior column (see black dashed line of B) overlying the region of activation (ROI, solid black lines) and covers a 55s period, either before activation, immediately upon activation and immediately post activation.
E. Diagram showing the regions analysed adjacent to the ROI. N indicates 'north', a region anterior to the ROI, S indicates 'south', a region posterior to the ROI, and E indicates 'east', a region medial to the ROI.
F. Polar plots showing the weighted average velocity direction during the first 55s of RhoA activation. Length of arrow indicates mean velocity (µm/min).
G. Absolute nuclei displacement in the AP axis in the 'north' or 'south' region of anteriorly or posteriorly directed embryos respectively, n = 62 nuclei from 10 embryos from 6 experiments. A statistical significant difference between groups was found using the Friedman test ($X2(2) = 11.6$, $p = 0.00296$) with significant differences between before and during (***$p = 0.0002$) and during and after (*$p = 0.036$) RhoA activation using the paired Wilcoxon signed-rank test with Bonferonni correction.
H.
    i. Average normalised velocity (relative to the preactivation mean) in the 'north' region of anteriorly directed 12-21 somite stage embryos, n = 6.
    ii. Average normalised velocity (relative to the preactivation mean) in the posterior region of posteriorly directed 13-15 somite stage embryos, n = 3.

I.

i. Average velocity direction (relative to the preactivation mean) in the 'north' region of anteriorly directed 12-21 somite stage embryos, n = 6, demonstrates a switch in mean direction towards the anterior during activation, and towards the posterior during deactivation of RhoA

ii. Average velocity direction (relative to the preactivation mean) in the 'south' region of posteriorly directed 13-15 somite stage embryos, n = 3, demonstrate a switch in mean direction towards the posterior during activation, and towards the anterior during deactivation of RhoA

J. Average velocity z-score in the anterior-posterior column overlying the ROI at the time of peak velocity for anteriorly directed embryos (i, n = 6) and posteriorly directed embryos (ii, n = 3), showing that the increase in velocity propagates along the anterior-posterior axis in the anterior (i) or posterior (ii) direction.

K. Average velocity in the 'north' or 'south' region of neural keel (12-15 somite stage embryos, n = 6) and neural rod (16-21 somite stage embryos, n = 4).

L. Peak velocity of in the 'north' or 'south' region of neural keel (12-15 somite stage embryos, n = 6) and neural rod (16-21 somite stage embryos, n = 4) is not significantly different. The peak velocities were not significantly difference using the two sample t test ($t(8) = 0.111$, $p = 0.915$).

Figure 6:

Oscillatory tissue expansion and contraction is sustained during RhoA activation and shear deformation is asymmetrically propagated

A. Cumulative isotropic strain rate during the first 55 seconds of activation. Representative image of an anteriorly directed 18 somite stage embryo.

B. Space-time heatmaps of isotropic strain rate z-score (average of anteriorly directed embryos, n = 7). Each panel represents an anterior-posterior column (see black dashed line of A) overlying the region of activation (ROI, solid black lines) and covers a 55s period, either before activation, immediately upon activation and immediately post activation.

C. Average isotropic strain rate z-score in the anterior-posterior column at the time of peak velocity during activation (average of anteriorly directed 12-21 somite stage embryos, n = 6).

D. Cumulative anisotropic strain rate during the first 55 seconds of activation. Representative image of an anteriorly directed 18 somite stage embryo.

E. Space-time heatmaps of anisotropic strain rate z-score (average of anteriorly directed 12-21 somite stage embryos, n = 7). Each panel represents an anterior-posterior column (see black dashed line of C) overlying the region of activation (ROI, solid black lines) and covers a 55s period, either before activation, immediately upon activation and immediately post activation.

F. Average anisotropic strain rate z-score in the anterior-posterior column at the time of peak velocity during activation (average of anteriorly directed 12-21 somite stage embryos, n = 6).

G. Raw anisotropic (pink) and isotropic (blue) strain rates in the anterior-posterior column at the time of peak velocity during activation showing that anisotropic strain has greater magnitude than isotropic strain (average of anteriorly directed 12-21 somite stage embryos, n = 6).

H. Isotropic strain rate amplitude before, during and after RhoA activation. One-way repeated measures ANOVA test showed no significance effect of RhoA activation on amplitude, ($F(2, 18) = 2.62$, $p = 0.1$).

I. Isotropic strain rate wavelength before, during and after RhoA activation. One-way repeated measures ANOVA test showed no significance effect of RhoA activation on wavelength, ($F(2, 18) = 1.87$, $p = 0.183$).

Figure 7:
Asymmetric response may be due to anterior-posterior gradients in nuclear density and RhoA activation

A. Average velocity direction and average normalised anisotropic and isotropic strain rates in the ROI before activation. Boxplots show median and upper/lower quartiles. Points indicate embryos (n = 6 and 3 for embryos that responded towards the anterior and posterior respectively). Watson two sample test (velocity direction, W = 0.1235, p > 0.10) and two-sample t tests (anisotropic and isotropic strain rate, (t(7) = -0.344, p = 0.741 and t(7) = -0.154, p = 0.882 respectively) show no significant difference between the anterior (pink) and posterior (blue) directed embryos.
B. Roseplot showing the mean vector direction within the combined NSE regions by rhombomere.
C. Nuclear density in the north and south regions of anteriorly or posteriorly directed embryos. Boxplots show median, upper and lower quartiles, points indicate individual embryos. Paired t-tests show no significant difference between north and south regions in anterior (t(9) = -1.38, p = 0.201) or posterior (t(2) = 1.15, p = 0.369) directed embryos
D. Gradients of Pif6-EGFP-LARG membrane/cytoplasm ratio across the AP axis of the ROI shows a correlation between gradient and directionality. Linear regression lines in colour show individual embryos, slope indicates the mean slope for each group.
E. Recruitment gradients for anterior and posterior directed embryos (colours as in D) did not show a significant difference using Wilcoxon rank sum test (W = 5, p = 0.0879).
F. Representative diagram showing membrane regions measured in the ROI during activation for Pif6-EGFP-LARG expression and before the timelapse experiment for PhyB-mCherry-Caax expression.
G. Lack of correlation between Pif6-EGFP-LARG gradient and PhyB-mCherry-Caax gradient. Points indicate individual embryos, colour matches with embryos in D. Spearman's rank correlation coefficient was not significant (rho = 0.086, p = 0.919).
H. Representative images of global optogenetic RhoA activation show preferential recruitment to cells undergoing mitosis and to the midline region in the neural keel and neural rod.
I. RhoA biosensor expression is elevated at the midline of the neural tissue.
    i. Mean ± SEM of the intensity of RhoA biosensor taken across the mediolateral (ML) width of the neural tissue, n = 4 embryos from neural keel (n = 2) to neural rod (n = 2) stage.
    ii. Representative images of neural keel and neural rod RhoA biosensor expression – dotted regions indicate line profiles taken for i.

References

Bailles A, Collinet C, Philippe JM, Lenne PF, Munro E, Lecuit T (2019) Genetic induction and mechanochemical propagation of a morphogenetic wave. *Nature* 572: 467-473

Balaji R, Bielmeier C, Harz H, Bates J, Stadler C, Hildebrand A, Classen AK (2017) Calcium spikes, waves and oscillations in a large, patterned epithelial tissue. *Sci Rep* 7: 42786

Balciunas D, Wangensteen KJ, Wilber A, Bell J, Geurts A, Sivasubbu S, Wang X, Hackett PB, Largaespada DA, McIvor RS *et al* (2006) Harnessing a high cargo-capacity transposon for genetic applications in vertebrates. *PLoS Genet* 2: e169

Bertet C, Sulak L, Lecuit T (2004) Myosin-dependent junction remodelling controls planar cell intercalation and axis elongation. *Nature* 429: 667-671

Bhattacharya D, Zhong J, Tavakoli S, Kabla A, Matsudaira P (2021) Strain maps characterize the symmetry of convergence and extension patterns during zebrafish gastrulation. *Sci Rep* 11: 19357

Buckley CE (2019) Optogenetic Control of Subcellular Protein Location and Signaling in Vertebrate Embryos. *Methods Mol Biol* 1920: 143-162

Buckley CE, Moore RE, Reade A, Goldberg AR, Weiner OD, Clarke JDW (2016) Reversible Optogenetic Control of Subcellular Protein Localization in a Live Vertebrate Embryo. *Dev Cell* 36: 117-126

Buckley CE, Ren X, Ward LC, Girdler GC, Araya C, Green MJ, Clark BS, Link BA, Clarke JD (2013) Mirror-symmetric microtubule assembly and cell interactions drive lumen formation in the zebrafish neural rod. *EMBO J* 32: 30-44

Castillo-Badillo JA, Bandi AC, Harlalka S, Gautam N (2020) SRRF-Stream Imaging of Optogenetically Controlled Furrow Formation Shows Localized and Coordinated Endocytosis and Exocytosis Mediating Membrane Remodeling. *ACS Synth Biol* 9: 902-919

Clarke DN, Martin AC (2021) Actin-based force generation and cell adhesion in tissue morphogenesis. *Curr Biol* 31: R667-R680

Countryman AD, Doherty CA, Herrera-Perez RM, Kasza KE (2024) Endogenous OptoRhoGEFs reveal biophysical principles of epithelial tissue furrowing. *bioRxiv*: 2024.2005.2012.593711

Crellin HA, Buckley CE (2024) Using Optogenetics to Investigate the Shared Mechanisms of Apical-Basal Polarity and Mitosis. *Cells Tissues Organs* 213: 161-180

De Belly H, Yan S, Borja da Rocha H, Ichbiah S, Town JP, Zager PJ, Estrada DC, Meyer K, Turlier H, Bustamante C *et al* (2023) Cell protrusions and contractions generate long-range membrane tension propagation. *Cell* 186: 3049-3061 e3015

Dicko M, Saramito P, Blanchard GB, Lye CM, Sanson B, Etienne J (2017) Geometry can provide long-range mechanical guidance for embryogenesis. *PLoS Comput Biol* 13: e1005443

Fernandez-Gonzalez R, Zallen JA (2011) Oscillatory behaviors and hierarchical assembly of contractile structures in intercalating cells. *Phys Biol* 8: 045005

Gibson DG, Young L, Chuang RY, Venter JC, Hutchison CA, 3rd, Smith HO (2009) Enzymatic assembly of DNA molecules up to several hundred kilobases. *Nat Methods* 6: 343-345

Gomez HF, Dumond MS, Hodel L, Vetter R, Iber D (2021) 3D cell neighbour dynamics in growing pseudostratified epithelia. *Elife* 10

Gustafson HJ, Claussen N, De Renzis S, Streichan SJ (2022) Patterned mechanical feedback establishes a global myosin gradient. *Nat Commun* 13: 7050

Hallett RA, Zimmerman SP, Yumerefendi H, Bear JE, Kuhlman B (2016) Correlating in Vitro and in Vivo Activities of Light-Inducible Dimers: A Cellular Optogenetics Guide. *ACS Synth Biol* 5: 53-64

He L, Wang X, Tang HL, Montell DJ (2010) Tissue elongation requires oscillating contractions of a basal actomyosin network. *Nat Cell Biol* 12: 1133-1142

Heisenberg CP, Bellaiche Y (2013) Forces in tissue morphogenesis and patterning. *Cell* 153: 948-962

Herrera-Perez RM, Cupo C, Allan C, Dagle AB, Kasza KE (2023) Tissue flows are tuned by actomyosin-dependent mechanics in developing embryos. *PRX Life* 1

Inman A, Lutton JE, Spiritosanto E, Tada M, Bretschneider T, Haas PA, Smutny M (2023) A multi-tiered mechanical mechanism shapes the early neural plate. *bioRxiv*: 2023.2006.2021.545965

Izquierdo E, Quinkler T, De Renzis S (2018) Guided morphogenesis through optogenetic activation of Rho signalling during early Drosophila embryogenesis. *Nat Commun* 9: 2366

Jaiswal M, Gremer L, Dvorsky R, Haeusler LC, Cirstea IC, Uhlenbrock K, Ahmadian MR (2011) Mechanistic insights into specificity, activity, and regulatory elements of the regulator of G-protein signaling (RGS)-containing Rho-specific guanine nucleotide exchange factors (GEFs) p115, PDZ-RhoGEF (PRG), and leukemia-associated RhoGEF (LARG). *J Biol Chem* 286: 18202-18212

Keller PJ, Schmidt AD, Wittbrodt J, Stelzer EH (2008) Reconstruction of zebrafish early embryonic development by scanned light sheet microscopy. *Science* 322: 1065-1069

Kimmel CB, Ballard WW, Kimmel SR, Ullmann B, Schilling TF (1995) Stages of embryonic development of the zebrafish. *Dev Dyn* 203: 253-310

Kindberg A, Hu JK, Bush JO (2020) Forced to communicate: Integration of mechanical and biochemical signaling in morphogenesis. *Curr Opin Cell Biol* 66: 59-68

Krueger D, Izquierdo E, Viswanathan R, Hartmann J, Pallares Cartes C, De Renzis S (2019) Principles and applications of optogenetics in developmental biology. *Development* 146

Krueger D, Tardivo P, Nguyen C, De Renzis S (2018) Downregulation of basal myosin-II is required for cell shape changes and tissue invagination. *EMBO J* 37

Mahlandt EK, Arts JJG, van der Meer WJ, van der Linden FH, Tol S, van Buul JD, Gadella TWJ, Goedhart J (2021) Visualizing endogenous Rho activity with an improved localization-based, genetically encoded biosensor. *J Cell Sci* 134

Martin AC, Kaschube M, Wieschaus EF (2009) Pulsed contractions of an actin-myosin network drive apical constriction. *Nature* 457: 495-499

Maves L, Jackman W, Kimmel CB (2002) FGF3 and FGF8 mediate a rhombomere 4 signaling activity in the zebrafish hindbrain. *Development* 129: 3825-3837

Mongera A, Pochitaloff M, Gustafson HJ, Stooke-Vaughan GA, Rowghanian P, Kim S, Campas O (2023) Mechanics of the cellular microenvironment as probed by cells in vivo during zebrafish presomitic mesoderm differentiation. *Nat Mater* 22: 135-143

Mongera A, Rowghanian P, Gustafson HJ, Shelton E, Kealhofer DA, Carn EK, Serwane F, Lucio AA, Giammona J, Campas O (2018) A fluid-to-solid jamming transition underlies vertebrate body axis elongation. *Nature* 561: 401-405

Natwick DE, Collins SR (2021) Optimized iLID Membrane Anchors for Local Optogenetic Protein Recruitment. *ACS Synth Biol* 10: 1009-1023

Nerurkar NL, Lee C, Mahadevan L, Tabin CJ (2019) Molecular control of macroscopic forces drives formation of the vertebrate hindgut. *Nature* 565: 480-484

Pannekoek WJ, de Rooij J, Gloerich M (2019) Force transduction by cadherin adhesions in morphogenesis. *F1000Res* 8

Petitjean L, Reffay M, Grasland-Mongrain E, Poujade M, Ladoux B, Buguin A, Silberzan P (2010) Velocity fields in a collectively migrating epithelium. *Biophys J* 98: 1790-1800

Peyret G, Mueller R, d'Alessandro J, Begnaud S, Marcq P, Mege RM, Yeomans JM, Doostmohammadi A, Ladoux B (2019) Sustained Oscillations of Epithelial Cell Sheets. *Biophys J* 117: 464-478

Rauzi M, Lenne PF, Lecuit T (2010) Planar polarized actomyosin contractile flows control epithelial junction remodelling. *Nature* 468: 1110-1114

Ruppel A, Worthmuller D, Misiak V, Kelkar M, Wang I, Moreau P, Mery A, Revilloud J, Charras G, Cappello G *et al* (2023) Force propagation between epithelial cells depends on active coupling and mechano-structural polarization. *Elife* 12

Sawyer JK, Choi W, Jung KC, He L, Harris NJ, Peifer M (2011) A contractile actomyosin network linked to adherens junctions by Canoe/afadin helps drive convergent extension. *Mol Biol Cell* 22: 2491-2508

Serra-Picamal X, Conte V, Vincent R, Anon E, Tambe DT, Bazellieres E, Butler JP, Fredberg JJ, Trepat X (2012) Mechanical waves during tissue expansion. *Nature Physics* 8: 628-634

Serrano Najera G, Weijer CJ (2020) Cellular processes driving gastrulation in the avian embryo. *Mech Dev* 163: 103624

Simoes Sde M, Blankenship JT, Weitz O, Farrell DL, Tamada M, Fernandez-Gonzalez R, Zallen JA (2010) Rho-kinase directs Bazooka/Par-3 planar polarity during Drosophila axis elongation. *Dev Cell* 19: 377-388

Symonds AC, Buckley CE, Williams CA, Clarke JDW (2020) Coordinated assembly and release of adhesions builds apical junctional belts during de novo polarisation of an epithelial tube. *Development* 147

Terriente J, Gerety SS, Watanabe-Asaka T, Gonzalez-Quevedo R, Wilkinson DG (2012) Signalling from hindbrain boundaries regulates neuronal clustering that patterns neurogenesis. *Development* 139: 2978-2987

Thomson L, Muresan L, Steventon B (2021) The zebrafish presomitic mesoderm elongates through compaction-extension. *Cells Dev* 168: 203748

Tlili S, Gauquelin E, Li B, Cardoso O, Ladoux B, Delanoe-Ayari H, Graner F (2018) Collective cell migration without proliferation: density determines cell velocity and wave velocity. *R Soc Open Sci* 5: 172421

Vanderleest TE, Xie Y, Budhathoki R, Linvill K, Hobson C, Heddleston J, Loerke D, Blankenship JT (2024) Lattice light sheet microscopy reveals 4D force propagation dynamics and leading-edge behaviors in an embryonic epithelium in Drosophila. *Curr Biol* 34: 3165-3177 e3163

Voelz D (2011) *Computational Fourier Optics: A MATLAB Tutorial, SPIE Press*
Wagner E, Glotzer M (2016) Local RhoA activation induces cytokinetic furrows independent of spindle position and cell cycle stage. *J Cell Biol* 213: 641-649

Westerfield M (2000) *The zebrafish book. A guide for the laboratory use of zebrafish (Danio rerio)*. Univ. of Oregon Press, Eugene.

Williams MLK, Solnica-Krezel L (2020) Cellular and molecular mechanisms of convergence and extension in zebrafish. *Curr Top Dev Biol* 136: 377-407

Zallen JA, Wieschaus E (2004) Patterned gene expression directs bipolar planar polarity in Drosophila. *Dev Cell* 6: 343-355